viruses

MDPI

Article

Subconfluent ARPE-19 Cells Display Mesenchymal Cell-State Characteristics and Behave like Fibroblasts, Rather than Epithelial Cells, in Experimental HCMV Infection Studies

Preethi Golconda, Mariana Andrade-Medina and Adam Oberstein *

Department of Microbiology and Immunology, College of Medicine, University of Illinois at Chicago, 835 South Wolcott Ave., Chicago, IL 60612, USA; pgolco2@uic.edu (P.G.); marianme@uic.edu (M.A.-M.)
* Correspondence: aoberste@uic.edu

Abstract: Human cytomegalovirus (HCMV) has a broad cellular tropism and epithelial cells are important physiological targets during infection. The retinal pigment epithelial cell line ARPE-19 has been used to model HCMV infection in epithelial cells for decades and remains a commonly used cell type for studying viral entry, replication, and the cellular response to infection. We previously found that ARPE-19 cells, despite being derived from an epithelial cell explant, express extremely low levels of canonical epithelial proteins, such as E-cadherin and EpCAM. Here, we perform comparative studies of ARPE-19 and additional epithelial cell lines with strong epithelial characteristics. We find that ARPE-19 cells cultured under subconfluent conditions resemble mesenchymal fibroblasts, rather than epithelial cells; this is consistent with previous studies showing that ARPE-19 cultures require extended periods of high confluency culture to maintain epithelial characteristics. By reanalyzing public gene expression data and using machine learning, we find evidence that ARPE-19 cultures maintained across many labs exhibit mesenchymal characteristics and that the majority of studies employing ARPE-19 use them in a mesenchymal state. Lastly, by performing experimental HCMV infections across mesenchymal and epithelial cell lines, we find that ARPE-19 cells behave like mesenchymal fibroblasts, producing logarithmic yields of cell-free infectious progeny, while cell lines with strong epithelial character exhibit an atypical infectious cycle and naturally restrict the production of cell-free progeny. Our work highlights important characteristics of the ARPE-19 cell line and suggests that subconfluent ARPE-19 cells may not be optimal for modeling epithelial infection with HCMV or other human viruses. It also suggests that HCMV biosynthesis and/or spread may occur quite differently in epithelial cells compared to mesenchymal cells. These differences could contribute to viral persistence or pathogenesis in epithelial tissues.

Keywords: herpesvirus; cytomegalovirus; human cytomegalovirus; HCMV; EMT; ARPE-19; MCF10A; RWPE-1

Citation: Golconda, P.; Andrade-Medina, M.; Oberstein, A. Subconfluent ARPE-19 Cells Display Mesenchymal Cell-State Characteristics and Behave like Fibroblasts, Rather than Epithelial Cells, in Experimental HCMV Infection Studies. *Viruses* **2024**, *16*, 49. https://doi.org/10.3390/v16010049

Academic Editors: Fenyong Liu and Ke Lan

Received: 2 November 2023
Revised: 20 December 2023
Accepted: 25 December 2023
Published: 28 December 2023

1. Introduction

Human cytomegalovirus (HCMV), a betaherpesvirus, is an important human pathogen with incompletely understood biology. The virus causes birth defects in newborns and morbidity in transplant patients, and is increasingly linked to chronic diseases, such as cancer or immune senescence. A vaccine for HCMV is not available and greater knowledge about HCMV biology is needed for continued therapeutic development.

Epithelial cells serve as primary targets for HCMV in the human body, playing pivotal roles in viral entry, dissemination, and the development of CMV-induced inflammatory diseases in various organs [1,2], including the intestine (CMV gastroenteritis), lungs (CMV pneumonia), and eyes (CMV retinitis) [1–4]. Furthermore, HCMV is suspected to establish persistent, possibly immunologically silent, infections in epithelial cells of the breast, kidney, and oral cavity [1,5–8].

The cell line ARPE-19 [9], derived from a primary human adult retinal pigment epithelium (RPE) explant, is commonly used to study HCMV in epithelial cells. ARPE-19 cells are not immortalized [9] but can be expanded substantially, thus providing a fairly stable source of retinal epithelial cells for functional and genetic studies. Additionally, they are both susceptible and permissive to HCMV infection [10,11] which makes them useful for studying mechanisms of entry, replication [12–17], and cellular responses to infection [10,18]. Since the virus is found in RPE cells during CMV retinitis [1,4,19–21], experimentally infected ARPE-19 cells are seen as a physiologically relevant in vitro model for studying HCMV in epithelial cells [22].

The majority of recent studies using ARPE-19 for modeling HCMV infection (including our own [10,11]) adsorb the virus onto just confluent or slightly subconfluent (e.g., 95% confluent) monolayers. However, ARPE-19 cells display density-dependent changes in their biochemistry [9,23,24]. For example, gene expression studies have shown large increases in the expression of visual cycle, melanogenesis, and epithelial junction genes after extended (four months), high-confluency culture [24]. Extended, high-confluency culture is also required for formation of tight-junctions, establishment of apico-basal polarization, and development of barrier function [9,25,26]. This functionally differentiated, high-density ARPE-19 state most resembles primary RPE [24,27]. Thus, it is possible that the low-confluency ARPE-19 cell state commonly used to study HCMV differs significantly from the physiologic epithelial state the virus encounters during natural infection in the eye.

In a previous study, we conducted comparative experimental infections with HCMV across ARPE-19 cells and permissive MRC-5 fibroblasts [10]. To our surprise, we observed that E-cadherin [28–31] and EpCAM [32–34], two canonical epithelial markers, were undetectable in uninfected ARPE-19 cells (see Figure 6E in [10]). Additionally, comprehensive transcriptomics analysis was unable to identify any significant cell type-specific responses to HCMV infection. These observations suggested that ARPE-19 cells were phenotypically similar to fibroblasts, rather than epithelial cells, raising concerns about their reliability as an epithelial infection model for HCMV. Given the known effects of cell density on ARPE-19 biology, we hypothesized that low-confluency culture (subculturing at 95% confluency) might encourage these cells to adopt a mesenchymal, rather than an epithelial, cell state.

Employing computational and genetic approaches, we have found that ARPE-19 cells maintained at subconfluency do indeed exhibit a mesenchymal, fibroblast-like phenotype that distinguishes them from typical epithelial cells. These properties are not specific to ARPE-19 cultures maintained in our laboratory, since reanalysis of RNA-sequencing data from a number of different laboratories shows nearly identical results. Genetic experiments involving epithelial and mesenchymal transcription factors have revealed that ARPE-19 cells possess limited plasticity to transition toward a further mesenchymal cell state but can readily transition to an epithelial state. This finding supports the notion that their baseline phenotype under subconfluent culture conditions tilts toward the mesenchymal end of the epithelial–mesenchymal axis. Furthermore, consistent with observations in the literature [24], prolonged growth at high confluency stimulated epithelial and RPE-specific gene expression, highlighting the dependency of epithelial features on cell density. However, long-term culture led to increased gene expression of both epithelial and mesenchymal genes, suggesting that even at high confluency, ARPE-19 cells may maintain a hybrid, potentially aberrant epithelial–mesenchymal cell state. Finally, by performing comparative experimental infections across ARPE-19 and strongly epithelial cell lines, we have found that ARPE-19 cells produce high yields of infectious progeny, similar to fibroblasts, while epithelial cell lines with strong epithelial characteristics display an atypical infectious cycle where cell-free infectious progeny production is strongly restricted.

Our findings underscore the significance of the epithelial–mesenchymal cell state axis as a potential modulator of HCMV infection. They also suggest that caution be exercised when using ARPE-19 cells to model epithelial infection with HCMV or other human viruses. We propose that the epithelial–mesenchymal cell state axis may serve as an intrinsic regulator of HCMV infection in epithelial cells, potentially influencing viral

biosynthesis, spread, or immune evasion, each of which could impact viral persistence or pathogenesis in epithelial tissues.

2. Materials and Methods

2.1. Cell Lines, Culture Conditions, and Viruses

MRC-5 embryonic lung fibroblasts, ARPE-19 adult retinal pigment epithelial cells, MCF10A mammary epithelial cells, and RWPE-1 prostate epithelial cells were obtained from the American Type Culture Collection. MRC-5 and ARPE-19 cells were grown in DMEM supplemented with 10% fetal bovine serum, 1 mM sodium pyruvate, 2 mM glutamax (Gibco, Grand Island, NY, USA), 10 mM Hepes pH 7.4, 0.1 mM MEM Non-Essential Amino Acids (Thermo Fisher Scientific, Waltham, MA, USA), 100 units/mL Penicillin G, and 100 µg/mL Streptomycin Sulfate. MCF10A cells were cultured in DMEM supplemented with 5% horse serum, 10 mM Hepes pH 7.4, 20 ng/mL EGF, 10 µg/mL Insulin, 1 nM Forskolin, 500 ng/mL Hydrocortisone, 100 units/mL Penicillin G, and 100 µg/mL Streptomycin Sulfate. RWPE-1 cells were cultured in K-SFM (Thermo Fisher Scientific, Waltham, MA, USA) supplemented with 25 units/mL Penicillin G and 25 µg/mL Streptomycin Sulfate. HCMV strain TB40/E-BAC4 [35] was reconstituted by electroporation into ARPE-19 cells. Virus stocks were titered on MRC-5 and ARPE-19 cells by an HCMV infectious unit assay (see below).

2.2. RNA-Sequencing Data Reanalysis

Public gene expression data were collected from the Gene Expression Omnibus (GEO) repository [36] (https://www.ncbi.nlm.nih.gov/geo/ (accessed on 11 October 2022)). Nine to eleven independent studies containing untreated or control-treated samples of MCF10A, RWPE-1, ARPE-19, and MRC-5 cells were manually identified and metadata from each study (Table S1) were uniformly curated to allow for automated download and processing. Raw reads from RNA-sequencing fastq files were pseudo-aligned to the homo sapiens transcriptome and converted to pseudo-counts using Kallisto [37]. Human genome release 34 (GRCh38.p13) was used for this analysis and reference transcripts and annotation metadata (gff3) were acquired from Genecode (https://www.gencodegenes.org/human/release_34.html (accessed on 20 August 2020)). The count matrices for all runs were joined and normalized for transcript length (within sample normalization) and compositional bias (cross-sample normalization) using the GeTMM [38] procedure and the R-package limma [39,40].

Hierarchical clustering was performed using the R-functions hclust from the R-package gplots [41] with method = "ward.D2" and distfun = function(x) as.dist(1-cor(t(x), method = "spearman")). Heatmaps were generated using the function heatmap.2 from the R-package gplots [41] and ggplot2 [42]. Cell type classification (epithelial vs. mesenchymal prediction) was performed in RR Core Team [43] using the MLseq [44] and caret [45] packages. Six different binary classifiers (Table 1) were trained on the GeTMM normalized count data for MCF10A, RWPE-1, and MRC-5, excluding ARPE-19 data, with MCF10A and RWPE-1 being assigned an "epithelial" (E) class label and MRC-5 being assigned a "mesenchymal" (M) class label. Tuning parameters were optimized using 5-fold cross-validation repeated 10 times. Accuracy was assessed by training on 70% of the input data (still excluding ARPE-19) and predicting the classes of the remaining 30%. All classifiers achieved 100% accuracy. Lastly, each trained model was used to predict the class of each ARPE-19 RNA-sequencing dataset, using the top 5000 most variable genes.

Table 1. Prediction of the ARPE-19 Phenotype Using Machine Learning Classification. Public gene expression data from Figures 1 and 2 were used to train six binary classifiers as described in Section 2. The proportion of RNA-seq runs predicted to be epithelial ("E") or mesenchymal ("M") is listed at the bottom of the table. Run IDs with hyphenated accession numbers are technical replicates used to increase RNA-sequencing coverage, which were concatenated and considered a single pooled sample.

		Predicted Phenotypic Class (E = Epithelial; M = Mesenchymal)					
RNA-Seq Run ID	**Cell Type**	**KNN**	**Logistic Regression**	**Naive Bayes**	**Support Vector Machine (Linear)**	**Support Vector Machine (Polynomial)**	**Random Forrest**
SRR5807527, -28, -29, -30	ARPE-19	M	M	M	M	M	M
SRR5807531, -32, -33, -34	ARPE-19	M	M	M	M	M	M
SRR5807535, -36, -37, -38	ARPE-19	M	M	M	M	M	M
SRR12193639	ARPE-19	M	M	M	M	M	M
SRR12193640	ARPE-19	M	M	M	M	M	M
SRR12193641	ARPE-19	M	M	M	M	M	M
SRR19895498, -99	ARPE-19	E	M	E	M	M	E
SRR19895500, -01	ARPE-19	M	M	M	M	M	M
SRR19895502, -03	ARPE-19	M	M	M	M	M	M
SRR5629569, -70	ARPE-19	M	M	M	M	M	M
SRR5629579, -80	ARPE-19	M	M	M	M	M	M
SRR19033104	ARPE-19	M	M	M	M	M	M
SRR19033105	ARPE-19	M	M	M	M	M	M
SRR19033106	ARPE-19	M	M	M	M	M	M
SRR8032314	ARPE-19	M	M	M	M	M	M
SRR8032315	ARPE-19	M	M	M	M	M	M
SRR8032316, -17	ARPE-19	M	M	M	M	M	M
SRR10766046	ARPE-19	E	M	M	M	M	M
SRR10766047	ARPE-19	E	M	M	M	M	M
SRR10766048	ARPE-19	E	M	M	M	M	M
SRR4427911	ARPE-19	M	M	M	M	M	M
SRR4427912	ARPE-19	M	M	M	M	M	M
SRR4427913	ARPE-19	M	M	M	M	M	M
SRR12795670	ARPE-19	M	M	M	M	M	M
SRR12795671	ARPE-19	M	M	M	M	M	M
Proportion Mesenchymal:		0.84	1.00	0.96	1.00	1.00	0.96

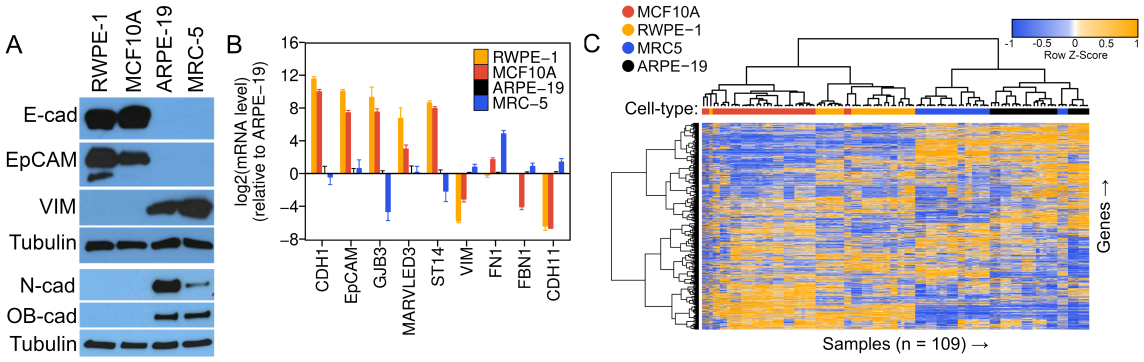

Figure 1. ARPE-19 Cells Display a Fibroblast-like, Mesenchymal Phenotype. (**A**) Western analysis of epithelial (E-cadherin, EpCAM) and mesenchymal (VIM, N-cadherin, OB-cadherin) marker proteins across RWPE-1, MCF10A, ARPE-19, and MRC-5 cell lines. β-Tubulin is shown as a loading control. (**B**) Relative mRNA levels of epithelial (*CDH1*, *EpCAM*, *GJB3*, *MARVELD3*, *ST14*) and mesenchymal

(*VIM, FN1, FBN1, CDH11*) marker genes measured by *q*RT-PCR. Data represent the mean +/− SD from three biological replicates assayed in technical triplicate. (**C**) Unsupervised clustering analysis of public gene expression data. One hundred and nine samples from 38 RNA-sequencing studies (see Table S1) of untreated or control-treated RWPE-1, MCF10A, ARPE-19, and MRC-5 cells were uniformly processed, normalized, clustered using 1-minus the Spearman's correlation coefficient as a distance metric (see Section 2), and displayed as a heatmap with dendrograms showing related clusters. Samples from the same cell types formed clusters and ARPE-19 cells established a clade with MRC5 cells, suggesting a similar global gene expression pattern.

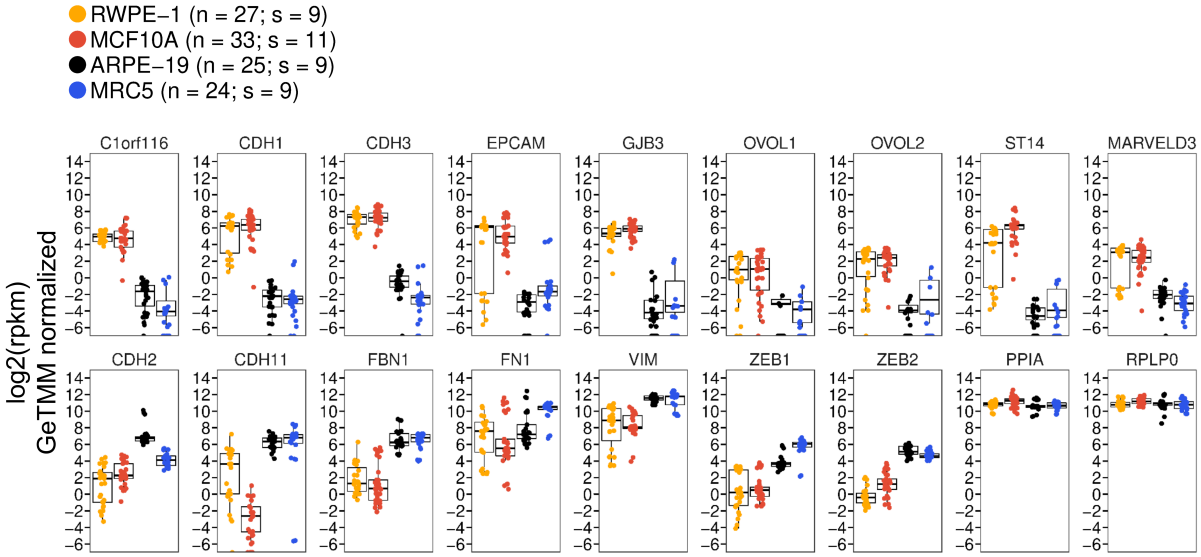

Figure 2. mRNA Expression Levels of Epithelial and Mesenchymal Genes from Public Transcriptomics Data. Relative expression levels of epithelial marker genes (**upper panel**), mesenchymal marker genes (**lower panel**, first seven plots), and normalization controls (*PPIA and RPLP0*). RNA-sequencing data were re-processed from the raw data from 38 studies, representing 109 sequencing runs (RWPE-19, n = 27; MCF10A, n = 33; ARPE-19, n = 25; MRC5, n = 24). Data represent the absolute expression level in reads-per-kilobase-per-million (rpkm) in each cell type, after cross-sample normalization of the 109 runs using the GeTMM procedure (see Section 2). Data are shown as strip plots with overlaid box-plots showing the median and interquartile range in each cell type. n = number of sequencing runs; s = number of studies.

2.3. HCMV Infectious Unit Assay

Supernatants from infected cells were collected, centrifuged at 500× g for 5 min to remove cellular debris, and serially diluted into complete media. For stock titration, 50 µL of concentrated HCMV particles were 10-fold serially diluted into virus storage buffer (PBS + 7% sucrose + 1% BSA) and 100 µL of each dilution was used to infect confluent monolayers of MRC-5 fibroblasts and ARPE-19 cells seeded into 24-well plates. At 20 hpi, cells were fixed with 100% methanol, stained for HCMV immediate early-1 (1E1) antigen using monoclonal antibody 1B12 [46], and imaged using a Keyence BZ-X710 Inverted Microscope. Wells with 20% or less infected nuclei were selected to avoid saturation effects. IE1-positive nuclei in each image were counted using CellProfiler [47] v2.1.1. The mean titer and standard deviation for each condition was calculated by multiplying the number of IE1-positive nuclei on each image by (1/dilution factor), (1.0 mL/infection volume) in milliliters, and a well factor. The well factor was the total well surface area (acquired from the plate manufacturer's engineering specification) divided by the image area (calculated using a calibration slide and the imageJ (Version 1.52) [48] function "set scale"). Four images/well (technical replicates) were sampled from three independent infections (biological replicates). Infectious units per mL (IU/mL) were determined by first

averaging the three technical replicates for each biological replicate (using the equation described above), converting each average to a titer, and then calculating the average and standard deviation of the biological replicates.

2.4. HCMV Growth Curves

Two days prior to infection, RWPE-1 cells were seeded into 24-well plates at 3×10^5/well. One day prior to infection, MCF10A, ARPE-19, and MRC-5 cells were seeded into 24-well plates at 2×10^5/well, 2×10^5/well, and 2.5×10^5/well, respectively. One 24-well plate per time point was seeded with triplicate wells of each cell type. The day of infection, cells were counted and media was changed to 0.7 mL complete media specific for each cell type (see Section 2.1). An identical HCMV virus stock was then added to triplicate wells of each cell type at an MOI of 1 IU/cell (MRC-5, ARPE-19, RWPE-1) or 3 IU/cell (MCF10A). Cultures were incubated at 37 °C/5% CO_2 for 2 h with gentle tapping every 30 min. At 2 hpi, monolayers were washed one time with warm PBS, 0.8 mL complete medium was added to each well, and cells were returned to the tissue culture incubator. At 1, 2, 3, 4, 5, and 6 days post-infection (dpi), cell supernatants were collected, cleared of detached cells by centrifuging at 300× *g* for 5 min at RT, aliquoted, and frozen at −80 °C until all time points were collected. Infected cell monolayers were washed with ice-cold PBS and harvested for Western analysis (see Section 2.8). Once all time points were harvested, supernatants were thawed (1 × freeze–thaw cycle), serially diluted in DMEM/10% FBS in 96-well plates, and adsorbed onto confluent monolayers of MRC-5 fibroblasts. Twenty-four hours later, reporter fibroblasts were fixed with cold MeOH and cell-free infectious progeny titers were determined using an infectious unit assay (see Section 2.3).

2.5. HCMV Entry Assay

The percentage of IE1-positive cells at 24 hpi was used to assess the frequency of infection with HCMV across the different cell lines, at different multiplicities of infection. Cells were seeded into 24-well plates in biological triplicate for each MOI and infected with HCMV as described above (see Section 2.4). At 24 hpi, monolayers were fixed in cold MeOH and stained for IE1 antigen using monoclonal antibody 1B12 [46]. Cells were counterstained with DAPI to visualize nuclei and the percentage of infected cells in each condition was calculated using fluorescence imaging. For quantification, nine random fields (technical replicates) were imaged in the IE1 and DAPI channels in each well. The percentage of infected cells in each field was calculated by dividing the number of IE1-positive nuclei by the total number of DAPI-positive, which were counted using CellProfiler [47] v2.1.1 software. The nine technical replicates were averaged to yield an estimate of the mean percentage of infected cells in each well, and then the "mean-of-means" and standard deviation were calculated across three independent infections (biological replicates) for each condition.

2.6. Vector and Stable Cell Line Construction

Sequence confirmed cDNAs encoding Snail and OVOL2 were obtained from the DNASU plasmid repository (Arizona State University, Tempe, AZ, USA) and subcloned into pLVX-TetOne-Puro (Takara Bio Inc., Shiga, Japan) vector. Lentiviral vectors were produced by co-transfecting each pLVX transfer vector with the packaging plasmids pCMV-dR8.91 and pCMV-VSV-G into HEK293FT cells. Plasmids were mixed in a 12:12:1 (vector:dR8.91:VSV-G) ratio by mass and mixed with an empirically optimized amount of branched polyethyleneimine (Sigma-Aldrich, St. Louis, MO, USA) before adding to cells. Lentivirus-containing supernatants were collected at 48 and 72 h post-transfection and concentrated over a 20% sorbitol cushion using ultracentrifugation. Lentivirus pellets were resuspended in PBS containing 7% Sucrose and 1% BSA. Transductions were performed by empirically determining the volume of lentivirus allowing 60 to 70% of the cells to survive puromycin selection; an effective MOI of approximately 1.0. 5 μg/mL hexadimethrine bromide ("polybrene"; Sigma-Aldrich, St. Louis, MO, USA) was added during transduction.

Forty-eight hours after transduction, selective media containing 2 µg/mL puromycin was added until non-transduced cells were completely killed, at which point transduced cells were maintained in 1 µg/mL puromycin for expansion. To induce Snail and OVOL2, cell populations were treated with either 1 µg/mL doxycycline for two to four days.

2.7. RNA-Preparation and Quantitative Reverse-Transcription PCR (qRT-PCR) Analysis

For *q*RT-PCR analysis, cells were collected in Tri-reagent (Sigma-Aldrich, St. Louis, MO, USA) and total RNA was isolated using an RNeasy RNA isolation kit (Qiagen, Germantown, MD, USA). DNA was removed using Turbo DNase (Thermo Fisher Scientific, Waltham, MA, USA) and RNA was quantified using a NanoDrop Spectrophotometer (Thermo Fisher Scientific, Waltham, MA, USA). cDNA was prepared using Superscript III reverse transcriptase (Thermo Fisher Scientific, Waltham, MA, USA) and random hexamer primers. *q*RT-PCR reactions were performed using Power SYBR Green Master Mix (Thermo Fisher Scientific, Waltham, MA, USA) and data were collected on a Viia7 digital PCR machine (Thermo Fisher Scientific, Waltham, MA, USA). Data were analyzed using the ΔΔCT method [49] with cyclophilin A (PPIA) as the reference gene. CDH1 and VIM primers were from Mani et al. [50]. All other primers were designed using either QuantPrime [51] or GETPRime [52]. *q*RT-PCR primer sequences are listed in Supplementary Table S2.

2.8. Western Blotting

For Western analysis, cell monolayers were collected in RIPA buffer (50 mM Hepes pH 7.4, 150 mM NaCl, 1% NP-40, 0.5% sodium deoxycholate, 0.1% SDS, 5 µg/mL aprotinin, 10 µg/mL leupeptin, 1 mM PMSF). Samples were then sonicated and debris was cleared by centrifugation. Protein concentration was determined using the BCA assay (Pierce) and equal amounts of total protein were separated by SDS-PAGE. Proteins were transferred to PVDF membranes and blocked with 5% BSA in HBST (50 mM Hepes pH 7.4, 150 mM NaCl, 0.05% tween-20). Primary antibodies (Supplementary Table S3) were diluted in 1% BSA and rocked at 4 °C overnight. Primary antibodies were detected using HRP-conjugated secondary antibodies and ECL Prime (Cytiva). Antibodies and dilutions are listed in Supplementary Table S3.

3. Results

3.1. The ARPE-19 Cell Line Exhibits Prominent Fibroblast-like, Mesenchymal Features

To corroborate the low baseline expression levels of E-cadherin and EpCAM in ARPE-19 cells and to gauge the expression range of these proteins in epithelial cells, we selected two widely employed epithelial cell lines from the biomedical literature as positive controls: MCF10A mammary epithelial cells [53] and RWPE-1 prostate epithelial cells [54]. MCF10A cells are spontaneously immortalized [53], while RWPE-1 cells have been immortalized using HPV-18 [54]. Both cell lines, however, remain untransformed and maintain stable epithelial morphology and functional characteristics in vitro [53–60]. HCMV has been found in both mammary epithelial cells [5] and prostate epithelial cells [61,62] in vivo; therefore, MCF10A and RWPE-1 are physiologically relevant experimental infection models. Our initial assessment involved comparing the steady-state expression levels of E-cadherin, EpCAM, and the mesenchymal marker Vimentin [63–66] across the epithelial control lines (MCF10A and RWPE-1), ARPE-19 cells, and MRC-5 fibroblast—a primary lung embryonic fibroblast culture serving as a mesenchymal control. As anticipated from our previous observations, E-cadherin and EpCAM were undetectable in ARPE-19 cells and MRC-5 fibroblasts, while the epithelial controls expressed high levels of both epithelial markers (Figure 1A). Conversely, steady-state levels of Vimentin, N-cadherin, and OB-cadherin were elevated in ARPE-19 and MRC-5 cells, yet undetectable in MCF10A and RWPE-1 (Figure 1A). To further substantiate these findings at the mRNA level and assess the expression of a broader panel of epithelial and mesenchymal markers, we conducted gene expression analysis across these cell lines. Quantitative reverse-transcription PCR (*q*RT-PCR) analysis revealed the following: (1) exceptionally high expression levels of epithelial genes in MCF10A and RWPE-1 compared to MRC-5 and

ARPE-19 cells (e.g., *CDH1*/E-cadherin mRNA was >4000-fold higher in MCF10A or RWPE-1 than in either MRC-5 or ARPE-19) (Figure 1B); (2) significantly higher levels of mesenchymal genes (e.g., *VIM, FBN1, CDH11*) in ARPE-19 and MRC-5 relative to MCF10A and RWPE-1 (Figure 1B); and (3) a gene expression pattern in ARPE-19 cells highly reminiscent of that in MRC-5 fibroblasts across most analyzed genes (Figure 1B). Hence, our Western blot (Figure 1A) and *q*RT-PCR (Figure 1B) analyses confirm that our ARPE-19 cells, analyzed immediately upon reaching confluency, assume a mesenchymal phenotype as opposed to an epithelial one.

Cell lines can exhibit phenotypic variations when maintained in different laboratories [67]. To address the potential for phenotypic drift in our specific ARPE-19 culture and comprehensively examine the hypothesis that commonly cultured ARPE-19 cells exhibit a mesenchymal phenotype, we conducted gene expression and classification analyses using publicly available transcriptomics data from MCF10A, RWPE-1, MRC-5, and ARPE-19 cells. Our goal was to establish a consensus transcriptomic signature for ARPE-19 cells by compiling data from numerous independent studies conducted in different laboratories. This entailed collecting data from nine to eleven distinct RNA-sequencing studies for each cell type, all sourced from the Gene Expression Omnibus [36] (GEO) (Table S1). In order to maximize the number of datasets from different labs, some control samples from perturbation experiments were included (e.g., siRNA control or vector controls); however, care was taken to acquire as many untreated RNA-seq runs for each cell type, wherever feasible. We uniformly processed and normalized the 109 individual samples collected from these studies (see Section 2) and conducted a comparative analysis on the resulting gene expression profiles. Our analysis comprised two primary components: (1) unsupervised hierarchical clustering to group samples based on their global gene expression patterns; and (2) supervised machine learning (ML) analysis to predict the epithelial-like (E) or mesenchymal-like (M) phenotype of ARPE-19 cells, employing ML classifiers trained on experimentally derived epithelial and mesenchymal gene expression profiles.

The hierarchical clustering definitively separated the four cell types into distinct clades (Figure 1C), indicating that the variation in gene expression due to batch effects, or other confounding variables, was minimal compared to the variation due to cell type identity. Two major phenotypic clades emerged, with ARPE-19 cells clustering closely with MRC-5 cells, and MCF10A cells clustering alongside RWPE-1 cells (Figure 1C). Analysis of individual epithelial and mesenchymal marker transcripts revealed that ARPE-19 displayed a gene expression pattern akin to that of MRC-5, with expression levels closely resembling those of MRC-5 cells and exhibiting an inverse correlation with those of MCF10A or RWPE-1 cells (Figure 2). For instance, *CDH1* and *EPCAM* exhibited extremely low mean expression levels (<1 rpkm) in both ARPE-19 and MRC-5 cells, while robust expression (between 32 and 64 rpkm) was observed in MCF10A and RWPE-1 cells. Conversely, mesenchymal markers, such as *CDH11, FBN1, VIM, ZEB1*, and *ZEB2*, displayed an opposite trend (Figure 2).

We next employed supervised ML techniques to predict the phenotypic class of ARPE-19 cells. For this analysis, we trained different binary ML classification models on a subset of the gene expression data used for clustering analysis (Table S1 and Figure 1C). To train these models, we removed the ARPE-19 samples from the normalized gene expression matrix and assigned an "M" or "E" class to each remaining sample (MRC-5 = M; MCF10A and RWPE-1 = E). Algorithms were then trained on 70% of the remaining data, and predictive accuracy was assessed by predicting the E vs. M class of the remaining 30%, still excluding ARPE-19. All models achieved 100% accuracy on the training data, as determined using a resampling (cross-validation) procedure (see Section 2). Each model was then used to predict the E vs. M class of each ARPE-19 sample. Using six different commonly used binary classifiers, the vast majority of ARPE-19 samples were projected to be mesenchymal (Table 1). Three out of the six classifiers predicted all ARPE-19 samples to be mesenchymal, while the remaining three classifiers predicted 96%, 96%, or 84% of the samples to be mesenchymal. These results align with the hierarchical clustering analysis and further affirm that ARPE-19 cells exhibit a mesenchymal phenotype closely resembling that of MRC-5. In summary, our analysis of public gene expression data substantiates

that ARPE-19 cells derived from multiple independent laboratories exhibit a mesenchymal phenotype akin to that of MRC-5, thereby validating our immunoblotting and *q*RT-PCR results characterizing our laboratory's ARPE-19 cell stock.

3.2. Subconfluent ARPE-19 Cells Are Inducible to an Epithelial Cell State but Not a Further Mesenchymal State

Most epithelial cells possess the capacity to transition between epithelial and mesenchymal cell states [30,68–71]. The well-characterized trans-differentiation process known as the epithelial-to-mesenchymal transition [30,71] (EMT) facilitates the conversion of static epithelial cells into migratory mesenchymal cells, while the reverse pathway, the mesenchymal-to-epithelial transition [72–76] (MET), reverts mesenchymal cells to an epithelial state. Both pathways play critical roles during tissue development, wound healing, and cancer development [30,68,71,77].

Intermediate states exhibiting features of both epithelial and mesenchymal cells have been documented [78–82], suggesting a continuum rather than discrete cell states along the epithelial–mesenchymal axis. To ascertain the position of ARPE-19 cells along this continuum, we explored the impact of expressing master regulator transcription factors associated with epithelial and mesenchymal states. We hypothesized that if ARPE-19 cells were genuinely mesenchymal, they would not readily transition to a further mesenchymal state through experimental manipulation but could be effectively induced into an epithelial state. To test this, we generated stable ARPE-19 and control MCF10A cell lines containing doxycycline (dox)-inducible versions of the EMT-inducing transcription factor Snail [83–86] or the MET-inducing transcription factor OVOL2 [76,87–90] (Figure 3A), and monitored phenotypic alterations in each cell population following the ectopic expression of Snail or OVOL2. In all experiments, comparison of parental cells in the presence and absence of dox ruled out spurious effects due to doxycycline, which have been observed in some systems [91–93]. Parental ARPE-19 cells exhibited a spindle-like, mesenchymal morphology using phase-contrast microscopy, unaffected by treatment with 1 µg/mL dox for 4 days (Figure 3B). Induction of Snail in ARPE-19 cells resulted in negligible change in cellular morphology, while the induction of OVOL2 led to the formation of clustered, cobblestone islands, a hallmark feature of differentiated epithelial cells (Figure 3B). Conversely, parental or uninduced MCF10A cells displayed a cobblestone morphology, transitioning to a spindle-like morphology with prominent extensions following ectopic expression of Snail, indicative of their conversion to a mesenchymal state. Additionally, MCF10A cells transitioned to an exaggerated cobblestone-island morphology after induction of OVOL2 (Figure 3B). These observations suggest that subconfluent ARPE-19 cells are closely aligned with a fully mesenchymal state on the epithelial–mesenchymal continuum, whereas MCF10A cells are situated closer to a fully epithelial state, with some capacity to transition to an exaggerated epithelial state.

To substantiate these findings, we assessed changes in epithelial and mesenchymal gene expression patterns in dox-treated (dox+) and vehicle-treated (dox-) cells using *q*RT-PCR (Figure 4A). MCF10A-iSnail cells treated with dox exhibited markedly reduced expression (16 to 32-fold) of epithelial genes (*CDH1*, *EPCAM*, *GJB3*, *MARVELD3*, *ST14*) and increased expression (up to 64-fold) of mesenchymal genes (*VIM*, *FN1*, *FBN1*) (Figure 4A). Conversely, MCF10A-iOVOL2 cells treated with dox displayed a modest elevation in epithelial gene expression (4- to 16-fold) and a decrease in mesenchymal gene expression (four- to nine-fold) (Figure 4B). ARPE-19-iSnail cells exhibited no statistically significant alterations in mesenchymal or epithelial gene expression upon dox treatment (Figure 4C). However, ARPE-19-iOVOL2 cells treated with dox showed a substantial increase in epithelial gene expression (e.g., 64-fold for *CDH1* or 128-fold for *EPCAM*) and reduced expression of mesenchymal genes such as *VIM* and *FBN1* (Figure 4D). Western analysis of E-cadherin, EpCAM, and Vimentin corroborated that changes in epithelial and mesenchymal gene expression were mirrored at the protein level (Figure 4E,F). These data confirm that ARPE-19 cells, when cultured under subconfluent conditions, exhibit a mesenchymal phenotype

with a high capacity to trans-differentiate into an epithelial state, contrary to MCF10A cells, which display a strong epithelial phenotype with potent trans-differentiation capacity towards a mesenchymal state. Combined with our computational analyses, these results affirm that ARPE-19 cells cultured under low-confluency conditions possess mesenchymal features, as opposed to epithelial features.

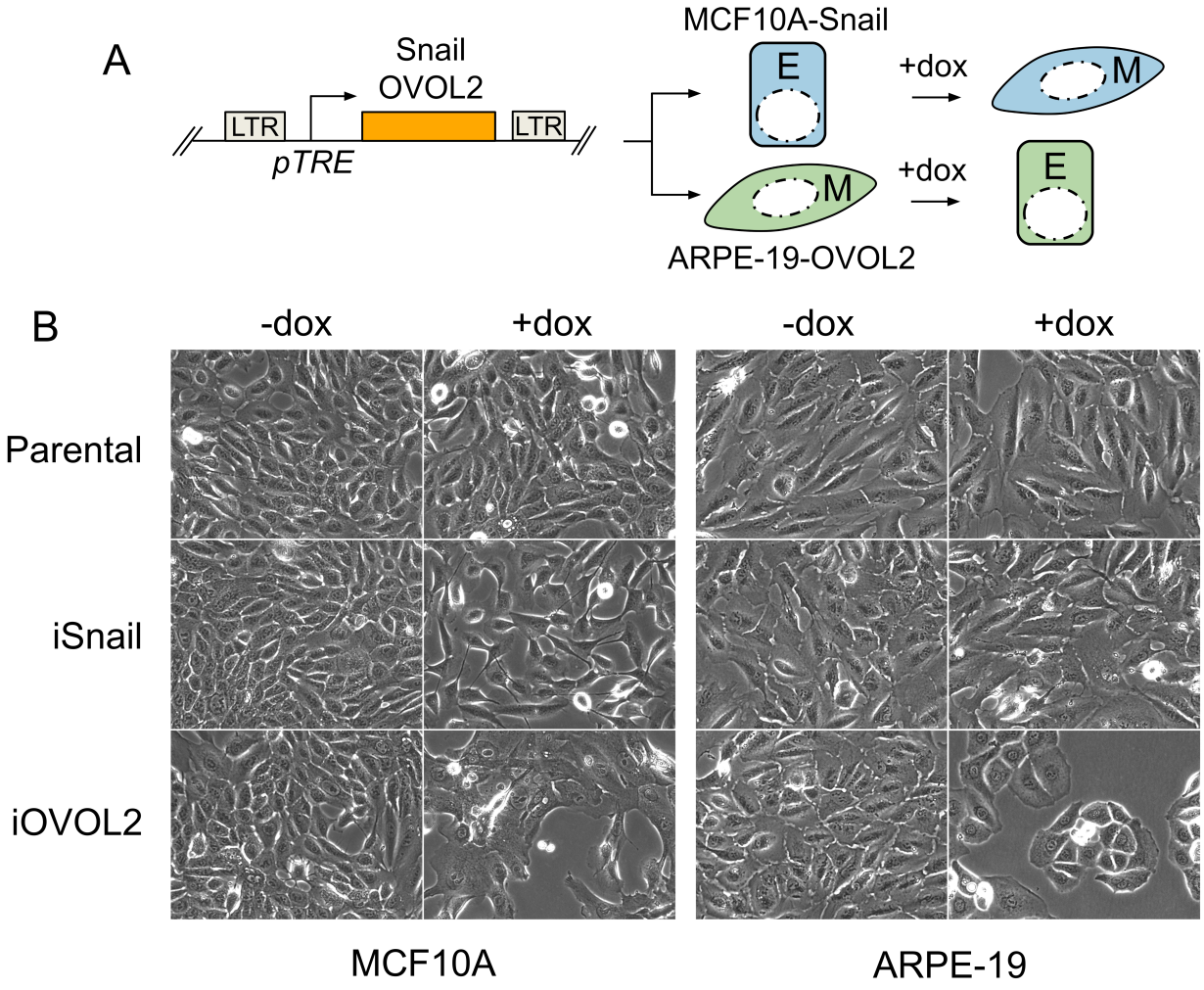

Figure 3. ARPE-19 Cells Show Morphological Features of Mesenchymal Cells and Can Be Driven to an Epithelial State Upon Expression of OVOL2. (**A**) Genetic system for assessing the impact of conditionally expressing EMT-inducing and MET-inducing transcription factors. The transcription factors Snail or OVOL2 are cloned into a doxycycline-inducible (dox), all-in-one lentiviral vector. Stable cell lines are established in MCF10A (MCF10A-iGeneX) or ARPE-19 (ARPE19-iGeneX) cells. Treatment with 1 μg/mL dox for 2–4 days drives cells toward a mesenchymal (Snail) or epithelial (OVOL2) cell fate and effects are observed. (**B**) Phase contrast images of showing morphological changes observed after 4 days of dox (1 μg/mL) treatment. MCF10A cells transition from a cobblestone epithelial morphology to a spindly mesenchymal morphology after expression of Snail. Parental ARPE19 cells display a mesenchymal morphology and show little-to-no morphological change after conditional expression of Snail, but can be driven towards a cobblestone epithelial morphology upon ectopic expression of OVOL2.

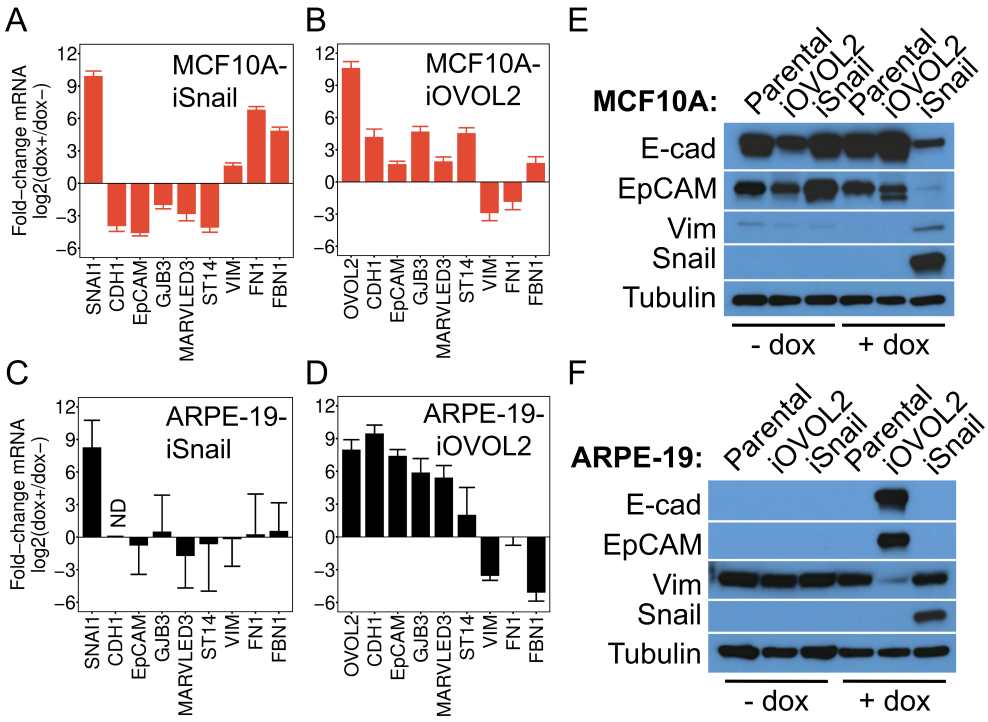

Figure 4. ARPE-19 Cells Can Be Experimentally Driven to an Epithelial Cell State by OVOL2, but Cannot Be Driven to a Further Mesenchymal State by Snail. Relative mRNA levels of epithelial (*CDH1, EpCAM, GJB3, MARVELD3, ST14*) and mesenchymal (*VIM, FN1, FBN1*) marker genes in MCF10A-iSnail (**A**), MCF10A-iOVOL2 (**B**), ARPE-19-iSnail (**C**), and ARPE-19-iOVOL2 (**D**) cells. Data were acquired using *q*RT-PCR and represent the fold-change in transcript levels after 4 days of treatment with 1 µg/mL dox or vehicle (water). Data represent the mean +/− SD from three biological replicates assayed in technical triplicate. CDH1 was undetectable ("ND" = not determined) in the experiment in panel C, before or after treatment with dox. (**E**,**F**) Western analysis of epithelial (E-cad, EpCAM) and mesenchymal (VIM) proteins in parental, iSnail, and iOVOL2 MCF10A (**E**) or ARPE-19 cells (**F**). *β*-Tubulin was used as a loading control.

3.3. Extended Confluent Culture Induces Epithelial and RPE-Specific Gene Expression in ARPE-19 Cells

Several studies have suggested that subculturing primary RPE [94,95] or ARPE-19 cells [24,95] at low confluency encourages an epithelial-to-mesenchymal transition (EMT). These studies demonstrated that the mesenchymal state associated with serial passaging could be reversed through extended maintenance (≥3 weeks) at high confluency [24] or transcription factor reprogramming [95]. This process caused increased expression of epithelial, visual-cycle, and RPE-signature genes [24,95]. We validated the induction of epithelial, visual-cycle, and RPE-signature genes in our lab stock of ARPE-19 cells over a three-week time course (Figure 5A,B). Interestingly, some mesenchymal genes such as FN1 and FBN1 were also elevated during this period (Figure 5A), suggesting that long-term cultured ARPE-19 cells may not fully transition to an epithelial state, but rather may attain a hybrid state embodying characteristics of both epithelial and mesenchymal cell states. Alternatively, even longer periods of confluent culture may be required to transition ARPE-19 cells to a fully differentiated epithelial cell state. Supporting this possibility, we were unable to detect the expression of the rate-limiting visual-cycle enzyme RPE65, known to be induced 10,000-fold following four months of high-confluency culture [24].

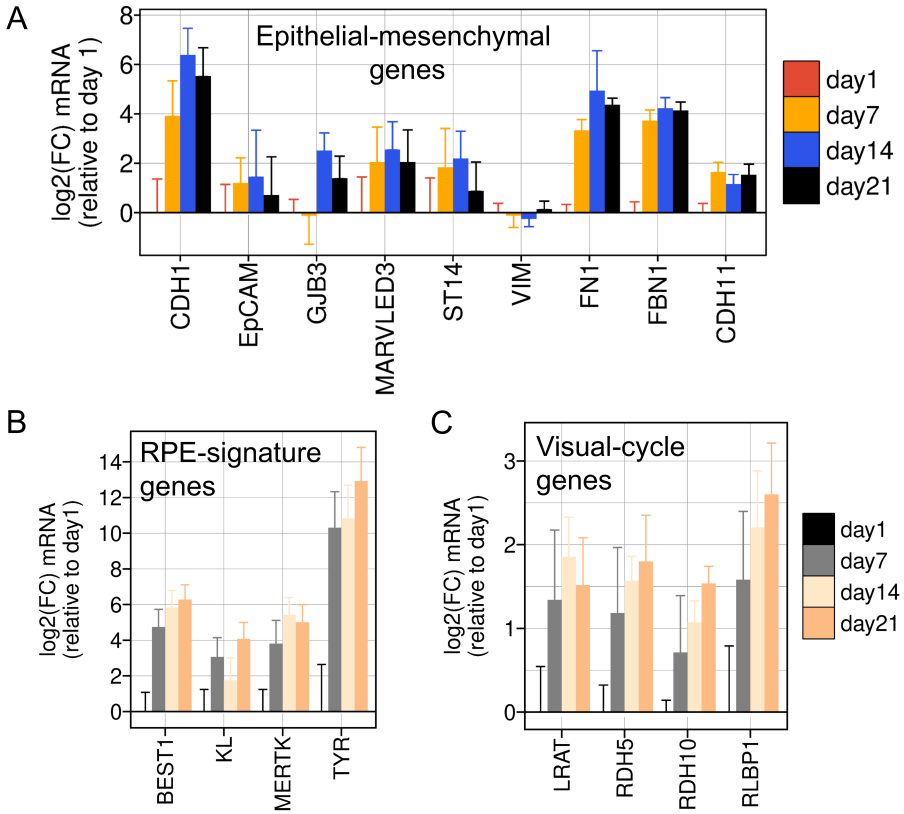

Figure 5. Gene Expression Changes Induced by Long-Term Culture of ARPE-19 Cells. Gene expression changes induced in ARPE-19 cells over three weeks of high-confluency culture. Total RNA was isolated at the indicated time points and reverse-transcribed, and relative mRNA levels were measured using quantitative RT-PCR (*q*RT-PCR). (**A**) Relative mRNA levels of epithelial (*CDH1, EpCAM, GJB3, MARVELD3, ST14*) and mesenchymal (*VIM, FN1, FBN1*) genes. (**B**) Relative mRNA levels of RPE-signature genes. (**C**) Relative mRNA levels of visual cycle genes responsible for retinol metabolism. Data represent the mean +/− SD from three biological replicates assayed in technical triplicate.

3.4. ARPE-19 Cells Phenocopy Fibroblasts in Experimental Infection Assays with Human Cytomegalovirus

Given our observations regarding the mesenchymal phenotype of ARPE-19 cells, we hypothesized that HCMV might behave differently in ARPE-19 than strongly epithelial cell lines in experimental infection studies. To test this possibility, we first determined the susceptibility of the epithelial cell lines MCF10A and RWPE-1 to HCMV infection. HCMV utilizes two glycoprotein complexes, termed "trimer" (gH, gL, gO) and "pentamer" (gH, gL, UL128, UL130, and UL131), to bind cellular entry receptors on various cell types [11,12,96–101]. ARPE-19, MCF10A, and RWPE-1 cells express low levels of PDGFR*α* mRNA (Figure 6A), the cellular receptor for the HCMV trimer. However, they do express entry factors for pentamer, including NRP2, TGFBR3, and CD46 (Figure 6A), suggesting that entry into these cell lines requires pentamer-containing strains of HCMV. Therefore, for this analysis, we employed HCMV strain TB40-BAC4 [35], which retains epithelial tropism and high levels of pentamer on virions when grown in ARPE-19 cells [10,11]. To assess susceptibility, we infected each cell line with HCMV at different MOIs and monitored IE1 expression at 24 hpi, a surrogate for viral entry. MRC-5 fibroblasts were used as fully susceptible control cells in these experiments. ARPE-19, MRC-5, and RWPE-1 cells were all highly susceptible to TB40-BAC4, with infection rates close to Poisson-theoretical (Figure 6B,C). MCF10A cells showed slightly reduced susceptibility, but more than 50% of the cells could be infected at a multiplicity of 3 IU/cell (Figure 6B,C).

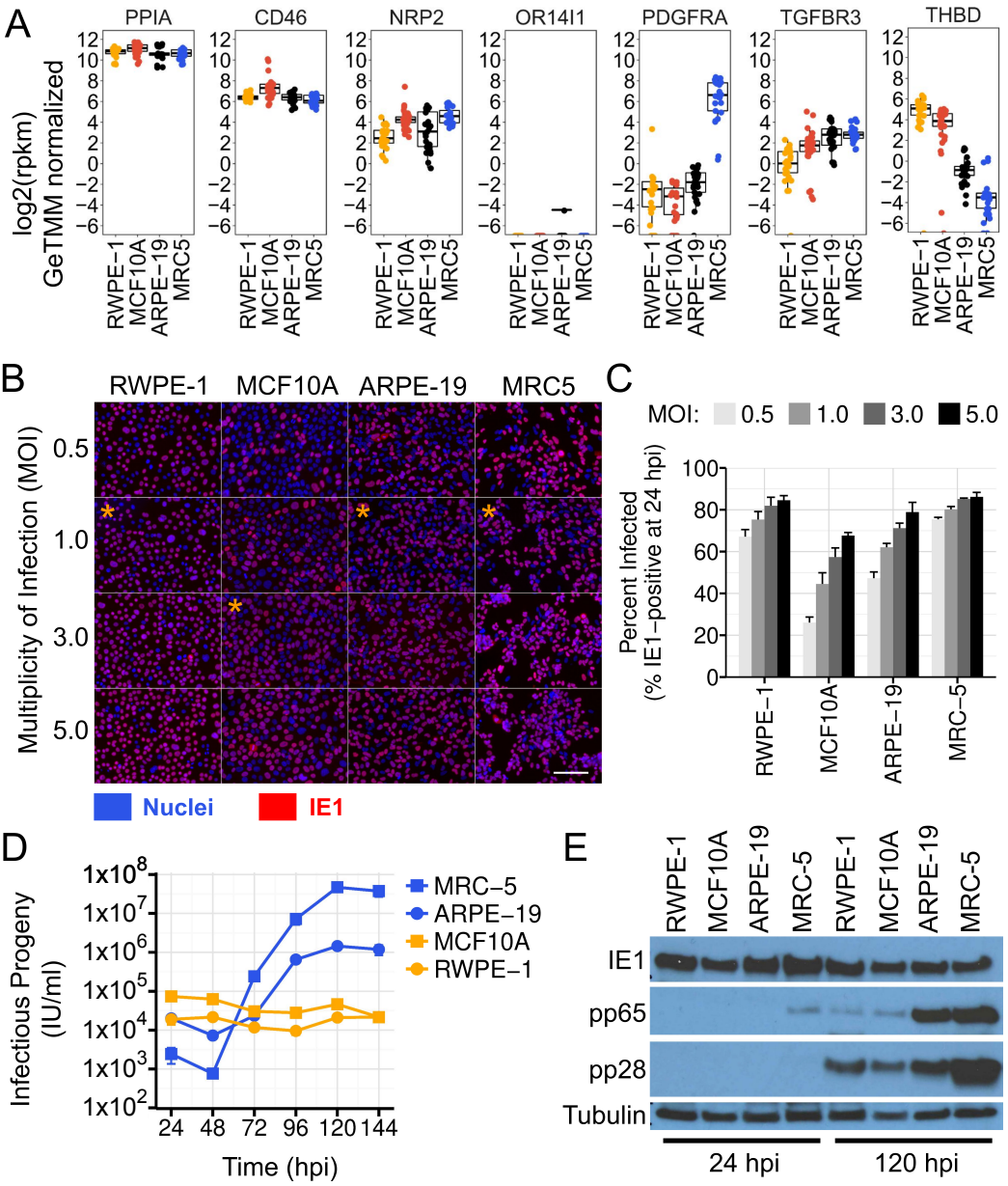

Figure 6. ARPE-19 Cells Phenocopy Fibroblasts in Experimental Infection Assays with Human Cytomegalovirus. (**A**) Absolute RNA-expression levels of HCMV entry factors across ARPE-19, MCR5, RWPE-1, and MCF10A cells. Data are normalized public gene expression data from Figures 1 and 2. PPIA RNA levels are shown as a normalization control. See Figure 2 and Section 2 for details. (**B**,**C**) HCMV susceptibility analysis. Fluorescence microscopy images of different cell types infected with HCMV TB40-BAC4 at various MOIs. IE1 (red) was visualized at 24 hpi by indirect immunofluorescence and nuclei were counterstained with DAPI (blue). Orange asterisks mark the MOIs used for growth curve analysis in panel *D*. Scale bar; 100 µm. The percentage of infected cells (**C**) was quantified for each cell type and multiplicity using Cellprofiler software (see Section 2). Data are mean +/− SD of three independent infections. (**D**) Single-step growth analysis of HCMV across four cell types. Infectious progeny released into the cell supernatants was assayed by IU-assay over a six-day time course. MRC-5, ARPE-19, and RWPE-1 cells were infected at 1 IU/cell. MCF10A cells were infected at 3 IU/cell. Data are mean +/− SD of three independent infections per cell type, per time point. In most cases, error bars are smaller than the data point symbols. (**E**) Immunoblot of HCMV proteins at 24 and 120 hpi, in infected epithelial and mesenchymal cell lines. Tubulin is shown as a loading control.

To assess permissivity and infectious progeny production, we next infected each cell line and monitored viral protein biosynthesis and infectious progeny production over a six-day infection time course. Each cell population was infected with an identical stock of HCMV TB40-BAC4 at a multiplicity of 1 IU/cell, with the exception of MCF10A cells, which were infected at 3 IU/cell to compensate for their reduced susceptibility. ARPE-19 cells produced logarithmically increasing yields of cell-free infectious progeny with similar kinetics to fully productive MRC-5 fibroblasts, although peak progeny yields were diminished by approximately 50-fold (Figure 6D). In contrast, MCF10A and RWPE-1 cells showed a reproductive index near unity, with only residual input infectivity recovered from the cell supernatants after six days of monitoring (Figure 6D). Analysis of steady-state viral protein levels in the infected cells from each population showed that the immediate-early protein IE1 was expressed at similar levels in all cell lines at 24 hpi, but late protein production was diminished late during infection (120 hpi), specifically in the epithelial cell lines (Figure 6D). Steady-state levels of the true-late protein pp28 were modestly reduced in RWPE-1 and MCF10A cells, while expression of the leaky-late protein pp65 was dramatically reduced (Figure 6D). It is not clear whether these alterations result from decreased mRNA or protein synthesis, or decreased stability. However, their occurrence specifically in the cell lines with strong epithelial character, which fail to produce infectious progeny, would seem to indicate the presence of cell type-specific mechanisms that strongly influence viral biosynthesis and/or spread.

Overall, these data show that HCMV behaves quite differently in ARPE-19 cells than strongly epithelial cell lines like MCF10A and RWPE-1. They also suggest that HCMV may establish a non-canonical pattern of infection in some epithelial cell types, where biosynthesis is atypical or delayed, or where the virus is transmitted without the production of cell-free progeny.

4. Discussion

The behavior of HCMV in epithelial cells has been a topic of interest in the HCMV field for some time. Early studies of HCMV infection in ARPE-19 or telomerase-immortalized RPE cells observed exclusive cell-associated replication, with little-to-no release of cell-free progeny and a low reproductive index (the ratio between input and output virus) [102,103]. However, these studies used HCMV propagated in human fibroblasts, which is known to decrease epithelial tropism [10,11,104–106]. Growth of clinical HCMV strains in ARPE-19 cells yields virions with epithelial-tropic properties, such as retention of high levels of the pentamer glycoproteins on virions [11] and a shift in entry route from endocytosis to direct-cell fusion [18]. These changes facilitate entry into a variety of epithelial and myeloid cell types [10,11], as well as the production of high yields of cell-free progeny in ARPE-19 cells [10]. A similar effect on HCMV tropism has been observed for stocks propagated in endothelial cells [35,104]. By preparing epithelial-tropic stocks of HCMV in ARPE-19 cells, we were able to compare HCMV permissivity across epithelial and mesenchymal cell lines using an identical virus preparation. We observed a strikingly different pattern of HCMV infection in mesenchymal and epithelial cells, with ARPE-19 cells behaving like productive fibroblasts, and epithelial cells displaying an atypical, potentially abortive, infection. The consequences and generality of this phenomenon are currently unknown. However, our realization that low-confluency ARPE-19 cultures typically lose their epithelial characteristics redirects future studies towards alternative epithelial cell models. In this regard, MCF10A and RWPE-1 cells could be helpful in dissecting how epithelial–mesenchymal cell states influence HCMV infection.

To the best of our knowledge, this is the first study to utilize MCF10A or RWPE-1 cells for experimental infection with HCMV. Both mammary epithelial cells and prostate epithelial cells are physiological sites of HCMV infection [5,61,62]. Therefore, these cell lines could be useful in future studies aimed at understanding HCMV replication in these cell types, both of which may harbor persistent HCMV in vivo.

ARPE-19 cells are a commonly used epithelial infection model for HCMV [17,18,107–122], as well as other human herpesviruses (e.g., VZV or HSV-1) [123–125], filoviruses (e.g., Ebola) [126], flaviviruses (e.g., Zika or Dengue) [127–129], and coronaviruses (e.g., SARS-CoV-2) [130]. Despite a number of studies showing that ARPE-19 requires prolonged periods of contact inhibited cell culture for functional differentiation [9,24], the use of undifferentiated, low-confluency ARPE-19 cultures (95% to just confluent) for infection studies is common. For example, we could find only one study in the HCMV literature explicitly stating that long-term, high-confluency culture was utilized [22], a study specifically designed to assess the effects of epithelial polarization on HCMV infection. The capacity of ARPE-19 to de-differentiate to a mesenchymal cell state in a density-dependent manner remains an underappreciated aspect of this cell line.

The data in this study provide clear evidence that low-confluency ARPE-19 cultures establish a mesenchymal, rather than epithelial, cell state. Using public gene expression data, we also provide evidence that this phenomenon pervades across a variety of studies using ARPE-19, suggesting that the loss of epithelial characteristics at low confluency is a general feature of the cell line, rather than a specific property of cultures maintained in our laboratory. Hopefully, this work will increase awareness of the cell state plasticity inherent to the ARPE-19 cell line, which continues to be an important in vitro model for studying retinal biology.

Is HCMV infection sensitive to the epithelial–mesenchymal cell state of cells? The answer to this question remains unclear. However, combining our observation that HCMV progeny production is restricted in some epithelial cell types with our previous data showing that HCMV infection itself can induce epithelial gene expression [10], it is possible that one or more features of the epithelial cell state program is intrinsically restrictive to HCMV, or alters the mode of transmission from cell-free to cell-associated. Alternatively, epithelial-specific transcriptional or translational mechanisms could control the kinetics of HCMV biosynthesis, potentially benefiting the virus by coordinating biosynthesis with intrinsic immune detection. Such a mechanism might explain the slow, persistent, infections thought to occur in some epithelial tissues. Modulating epithelial cell state features via the epithelial-to-mesenchymal transition (EMT) and observing the effects on HCMV biosynthesis and spread could be useful for studying how epithelial–mesenchymal cell states impact the HCMV infectious cycle. Ultimately, however, more sophisticated animal models will be required to determine whether epithelial–mesenchymal cell state dynamics influence natural infections in vivo.

One limitation of our study is that we have only assessed HCMV infection in a small number of epithelial cell lines. It will be important to extend these observations to additional epithelial cell types in the future to determine whether our results generalize across diverse epithelial cell types or are specific to the particular mammary and prostate cell lines we have tested.

5. Conclusions

Overall, our results indicate that subconfluent ARPE-19 cells are not ideal for studying HCMV interactions with epithelial cells in vitro, and unveil the epithelial–mesenchymal cell state axis as a potential regulator of HCMV infection in epithelial cells. Our findings also underscore the necessity for caution when utilizing density-dependent cell lines such as ARPE-19 for cell biological experiments. We hope that our work serves to inform future studies utilizing ARPE-19 cells as a model for epithelial infections, not only with HCMV but also with other human pathogens.

Supplementary Materials: The following supporting information can be downloaded at: https://www.mdpi.com/article/10.3390/v16010049/s1, Table S1: Public RNA-seq metadata used in this study.; Table S2: qRT-PCR primers used in this study.; Table S3: Antibodies used in this study.

Author Contributions: Conceptualization, P.G. and A.O.; methodology, P.G., M.A.-M. and A.O.; validation, P.G., M.A.-M. and A.O.; formal analysis, P.G., M.A.-M. and A.O; data curation, A.O.; writing—original draft preparation, P.G. and A.O.; writing—review and editing, P.G. and A.O.; supervision, A.O.; project administration, A.O.; funding acquisition, A.O. All authors have read and agreed to the published version of the manuscript.

Funding: Funding for this work was provided to A.O. by UIC College of Medicine Startup Funds. This research received no external funding.

Institutional Review Board Statement: Not applicable.

Informed Consent Statement: Not applicable.

Data Availability Statement: Kallisto pseudo-counts, study metadata, and count matrices; code used to perform normalization, clustering, and machine learning analyses; and data visualization are available at the following public github repository: https://github.com/aoberstein/2023-Golconda_A19_paper.git.

Acknowledgments: We thank Alan McLachlan, (UIC) for critical reading of our manuscript and general support, Thomas Shenk, (Princeton University) for advice and providing the HCMV monoclonal antibodies used in this study, and the UIC College of Medicine for providing funding for this research.

Conflicts of Interest: The authors declare no conflicts of interest.

Abbreviations

The following abbreviations are used in this manuscript:

HCMV	Human Cytomegalovirus
EMT	Epithelial-to-mesenchymal Transition
*q*RT-PCR	Quantitative real-time PCR
dox	doxycycline
MOI	Multiplicity of infection
dpi	Days post-infection
hpi	Hours post-infection

References

1. Britt, W. Manifestations of human cytomegalovirus infection: Proposed mechanisms of acute and chronic disease. In *Human Cytomegalovirus*; Shenk, T., Stinski, M., Eds.; Springer: Berlin/Heidelberg, Germany 2008; pp. 417–470.
2. Sinzger, C.; Digel, M.; Jahn, G. Cytomegalovirus Cell Tropism. In *Human Cytomegalovirus*; Current Topics in Microbiology and Immunology; Shenk, T.E., Stinski, M.F., Eds.; Springer: Berlin/Heidelberg, Germany, 2008; Volume 325, pp. 63–83. [CrossRef]
3. Goodrum, F.; Caviness, K.; Zagallo, P. Human cytomegalovirus persistence. *Cell. Microbiol.* **2012**, *14*, 644–655. [CrossRef] [PubMed]
4. Mocarski, E.; Shenk, T.; Griffiths, P.; Pass, R. Cytomegaloviruses. In *Fields Virology*, 6th ed.; Knipe, D., Howley, P., Eds.; Wolters Kluwer Lippincott Williams & Wilkins: Philadelphia, PA, USA, 2013; pp. 1960–2014.
5. Harkins, L.E.; Matlaf, L.A.; Soroceanu, L.; Klemm, K.; Britt, W.J.; Wang, W.; Bland, K.I.; Cobbs, C.S. Detection of human cytomegalovirus in normal and neoplastic breast epithelium. *Herpesviridae* **2010**, *1*, 8. [CrossRef] [PubMed]
6. Moussawi, F.A.; Kumar, A.; Pasquereau, S.; Tripathy, M.K.; Karam, W.; Diab-Assaf, M.; Herbein, G. The transcriptome of human mammary epithelial cells infected with the HCMV-DB strain displays oncogenic traits. *Sci. Rep.* **2018**, *8*, 12574. [CrossRef]
7. Rabe, T.; Lazar, K.; Cambronero, C.; Goelz, R.; Hamprecht, K. Human Cytomegalovirus (HCMV) Reactivation in the Mammary Gland Induces a Proinflammatory Cytokine Shift in Breast Milk. *Microorganisms* **2020**, *8*, 289. [CrossRef] [PubMed]
8. Weng, C.; Lee, D.; Gelbmann, C.B.; Sciver, N.V.; Nawandar, D.M.; Kenney, S.C.; Kalejta, R.F. Human Cytomegalovirus Productively Replicates In Vitro in Undifferentiated Oral Epithelial Cells. *J. Virol.* **2018**, *92*, e00903-18. [CrossRef]
9. Dunn, K.; Aotaki-Keen, A.; Putkey, F.; Hjelmeland, L. ARPE-19, A Human Retinal Pigment Epithelial Cell Line with Differentiated Properties. *Exp. Eye Res.* **1996**, *62*, 155–170. [CrossRef]
10. Oberstein, A.; Shenk, T. Cellular responses to human cytomegalovirus infection: Induction of a mesenchymal-to-epithelial transition (MET) phenotype. *Proc. Natl. Acad. Sci. USA* **2017**, *114*, E8244–E8253. [CrossRef]
11. Wu, K.; Oberstein, A.; Wang, W.; Shenk, T. Role of PDGF receptor-α during human cytomegalovirus entry into fibroblasts. *Proc. Natl. Acad. Sci. USA* **2018**, *115*, E9889–E9898. [CrossRef]
12. Liu, J.; Jardetzky, T.S.; Chin, A.L.; Johnson, D.C.; Vanarsdall, A.L. The Human Cytomegalovirus Trimer and Pentamer Promote Sequential Steps in Entry into Epithelial and Endothelial Cells at Cell Surfaces and Endosomes. *J. Virol.* **2018**, *92*, 1110–1128. [CrossRef]

13. Martinez-Martin, N.; Marcandalli, J.; Huang, C.S.; Arthur, C.P.; Perotti, M.; Foglierini, M.; Ho, H.; Dosey, A.M.; Shriver, S.; Payandeh, J.; et al. An Unbiased Screen for Human Cytomegalovirus Identifies Neuropilin-2 as a Central Viral Receptor. *Cell* **2018**, *174*, 1158–1171.e19. [CrossRef]
14. Stein, K.R.; Gardner, T.J.; Hernandez, R.E.; Kraus, T.A.; Duty, J.A.; Ubarretxena-Belandia, I.; Moran, T.M.; Tortorella, D. CD46 facilitates entry and dissemination of human cytomegalovirus. *Nat. Commun.* **2019**, *10*, 1–13. [CrossRef]
15. Vanarsdall, A.L.; Pritchard, S.R.; Wisner, T.W.; Liu, J.; Jardetzky, T.S.; Johnson, D.C. CD147 Promotes Entry of Pentamer-Expressing Human Cytomegalovirus into Epithelial and Endothelial Cells. *mBio* **2018**, *9*, e00781-18. [CrossRef]
16. Vanarsdall, A.L.; Wisner, T.W.; Lei, H.; Kazlauskas, A.; Johnson, D.C. PDGF Receptor-α Does Not Promote HCMV Entry into Epithelial and Endothelial Cells but Increased Quantities Stimulate Entry by an Abnormal Pathway. *PLoS Pathog.* **2012**, *8*, e1002905. [CrossRef]
17. Ye, X.; Su, H.; Wrapp, D.; Freed, D.C.; Li, F.; Yuan, Z.; Tang, A.; Li, L.; Ku, Z.; Xiong, W.; et al. Recognition of a highly conserved glycoprotein B epitope by a bivalent antibody neutralizing HCMV at a post-attachment step. *PLoS Pathog.* **2020**, *16*, e1008736. [CrossRef]
18. Wang, D.; Yu, Q.C.; Schröer, J.; Murphy, E.; Shenk, T. Human cytomegalovirus uses two distinct pathways to enter retinal pigmented epithelial cells. *Proc. Natl. Acad. Sci. USA* **2007**, *104*, 20037–20042. [CrossRef]
19. Egbert, P.R. Cytomegalovirus Retinitis in Immunosuppressed Hosts: II. Ocular Manifestations. *Ann. Intern. Med.* **1980**, *93*, 664. [CrossRef]
20. Pepose, J.S.; Newman, C.; Bach, M.C.; Quinn, T.C.; Ambinder, R.F.; Holland, G.N.; Hodstrom, P.S.; Frey, H.M.; Foos, R.Y. Pathologic Features of Cytomegalovirus Retinopathy after Treatment with the Antiviral Agent Ganciclovir. *Ophthalmology* **1987**, *94*, 414–424. [CrossRef]
21. Rao, N.A.; Zhang, J.; Ishimoto, S. Role of retinal vascular endothelial cells in development of CMV retinitis. *Trans. Am. Ophthalmol. Soc.* **1998**, *96*, 111–126. [PubMed]
22. Tugizov, S.; Maidji, E.; Pereira, L. Role of apical and basolateral membranes in replication of human cytomegalovirus in polarized retinal pigment epithelial cells. *J. Gen. Virol.* **1996**, *77*, 61–74. [CrossRef] [PubMed]
23. Al-Ani, A.; Sunba, S.; Hafeez, B.; Toms, D.; Ungrin, M. In Vitro Maturation of Retinal Pigment Epithelium Is Essential for Maintaining High Expression of Key Functional Genes. *Int. J. Mol. Sci.* **2020**, *21*, 6066. [CrossRef] [PubMed]
24. Samuel, W.; Jaworski, C.; Postnikova, O.A.; Kutty, R.K.; Duncan, T.; Tan, L.X.; Poliakov, E.; Lakkaraju, A.; Redmond, T.M. Appropriately differentiated ARPE-19 cells regain phenotype and gene expression profiles similar to those of native RPE cells. *Mol. Vis.* **2017**, *23*, 60–89. [PubMed]
25. Ablonczy, Z.; Dahrouj, M.; Tang, P.H.; Liu, Y.; Sambamurti, K.; Marmorstein, A.D.; Crosson, C.E. Human Retinal Pigment Epithelium Cells as Functional Models for the RPE In Vivo. *Investig. Ophthalmol. Vis. Sci.* **2011**, *52*, 8614–8620. [CrossRef] [PubMed]
26. Luo, Y.; Zhuo, Y.; Fukuhara, M.; Rizzolo, L.J. Effects of Culture Conditions on Heterogeneity and the Apical Junctional Complex of the ARPE-19 Cell Line. *Investig. Ophthalmol. Vis. Sci.* **2006**, *47*, 3644–3655. [CrossRef] [PubMed]
27. Tian, J. The expression of native and cultured human retinal pigment epithelial cells grown in different culture conditions. *Br. J. Ophthalmol.* **2005**, *89*, 1510–1517. [CrossRef] [PubMed]
28. Bracke, M.E.; Roy, F.M.V.; Mareel, M.M. The E-cadherin/Catenin Complex in Invasion and Metastasis. In *Attempts to Understand Metastasis Formation I: Metastasis-Related Molecules*; Current Topics in Microbiology 213/I and Immunology; Günthert, U., Birchmeier, W., Eds.; Springer: Berlin/Heidelberg, Germany, 1996; p. 123–161. [CrossRef]
29. Frixen, U.H.; Behrens, J.; Sachs, M.; Eberle, G.; Voss, B.; Warda, A.; Lochner, D.; Birchmeier, W. E-cadherin-mediated cell-cell adhesion prevents invasiveness of human carcinoma cells. *J. Cell Biol.* **1991**, *113*, 173–185. [CrossRef] [PubMed]
30. Kalluri, R.; Weinberg, R.A. The basics of epithelial-mesenchymal transition. *J. Clin. Investig.* **2009**, *119*, 1420–1428. [CrossRef] [PubMed]
31. Onder, T.T.; Gupta, P.B.; Mani, S.A.; Yang, J.; Lander, E.S.; Weinberg, R.A. Loss of E-Cadherin Promotes Metastasis via Multiple Downstream Transcriptional Pathways. *Cancer Res.* **2008**, *68*, 3645–3654. [CrossRef] [PubMed]
32. Gires, O.; Pan, M.; Schinke, H.; Canis, M.; Baeuerle, P.A. Expression and function of epithelial cell adhesion molecule EpCAM: where are we after 40 years? *Cancer Metastasis Rev.* **2020**, *39*, 969–987. [CrossRef]
33. Schnell, U.; Cirulli, V.; Giepmans, B.N. EpCAM: Structure and function in health and disease. *Biochim. Biophys. Acta (BBA)-Biomembr.* **2013**, *1828*, 1989–2001. [CrossRef]
34. Slanchev, K.; Carney, T.J.; Stemmler, M.P.; Koschorz, B.; Amsterdam, A.; Schwarz, H.; Hammerschmidt, M. The Epithelial Cell Adhesion Molecule EpCAM Is Required for Epithelial Morphogenesis and Integrity during Zebrafish Epiboly and Skin Development. *PLoS Genet.* **2009**, *5*, e1000563. [CrossRef]
35. Sinzger, C.; Hahn, G.; Digel, M.; Katona, R.; Sampaio, K.L.; Messerle, M.; Hengel, H.; Koszinowski, U.; Brune, W.; Adler, B. Cloning and sequencing of a highly productive, endotheliotropic virus strain derived from human cytomegalovirus TB40/E. *J. Gen. Virol.* **2008**, *89*, 359–368. [CrossRef] [PubMed]
36. Barrett, T.; Wilhite, S.E.; Ledoux, P.; Evangelista, C.; Kim, I.F.; Tomashevsky, M.; Marshall, K.A.; Phillippy, K.H.; Sherman, P.M.; Holko, M.; et al. NCBI GEO: Archive for functional genomics data sets—Update. *Nucleic Acids Res.* **2013**, *41*, D991–D995. [CrossRef] [PubMed]

37. Bray, N.L.; Pimentel, H.; Melsted, P.; Pachter, L. Near-optimal probabilistic RNA-seq quantification. *Nat. Biotechnol.* **2016**, *34*, 525–527. [CrossRef] [PubMed]
38. Smid, M.; Coebergh van den Braak, R.R.J.; van de Werken, H.J.G.; van Riet, J.; van Galen, A.; de Weerd, V.; van der Vlugt-Daane, M.; Bril, S.I.; Lalmahomed, Z.S.; Kloosterman, W.P.; et al. Gene length corrected trimmed mean of M-values (GeTMM) processing of RNA-seq data performs similarly in intersample analyses while improving intrasample comparisons. *BMC Bioinform.* **2018**, *19*, 236. [CrossRef] [PubMed]
39. Ritchie, M.E.; Phipson, B.; Wu, D.; Hu, Y.; Law, C.W.; Shi, W.; Smyth, G.K. limma powers differential expression analyses for RNA-sequencing and microarray studies. *Nucleic Acids Res.* **2015**, *43*, e47. [CrossRef]
40. Smyth, G.K. Linear models and empirical Bayes methods for assessing differential expression in microarray experiments. *Stat. Appl. Genet. Mol. Biol.* **2004**, *3* . [CrossRef]
41. Warnes, G.R.; Bolker, B.; Bonebakker, L.; Gentleman, R.; Liaw, W.H.A.; Lumley, T.; Maechler, M.; Magnusson, A.; Moeller, S.; Schwartz, M.; et al. gplots: Various R Programming Tools for Plotting Data. 2016. Available online: https://cran.r-project.org/web/packages/gplots/gplots.pdf (accessed on 1 November 2023).
42. Wickham, H. *ggplot2: Elegant Graphics for Data Analysis*; Springer: New York, NY, USA, 2016.
43. R Core Team. *R A Language and Environment for Statistical Computing*; R Foundation for Statistical Computing: Vienna, Austria, 2020.
44. Goksuluk, D.; Zararsiz, G.; Korkmaz, S.; Eldem, V.; Zararsiz, G.E.; Ozcetin, E.; Ozturk, A.; Karaagaoglu, A.E. MLSeq: Machine learning interface for RNA-sequencing data. *Comput. Methods Programs Biomed.* **2019**, *175*, 223–231. [CrossRef]
45. Kuhn, M. Caret: Classification and Regression Training. 2022. Available online: https://cran.r-project.org/web/packages/caret/caret.pdf (accessed on 1 November 2023).
46. Zhu, H.; Shen, Y.; Shenk, T. Human cytomegalovirus IE1 and IE2 proteins block apoptosis. *J. Virol.* **1995**, *69*, 7960–7970. [CrossRef]
47. Carpenter, A.E.; Jones, T.R.; Lamprecht, M.R.; Clarke, C.; Kang, I.H.; Friman, O.; Guertin, D.A.; Chang, J.H.; Lindquist, R.A.; Moffat, J.; et al. CellProfiler: Image analysis software for identifying and quantifying cell phenotypes. *Genome Biol.* **2006**, *7*, R100. [CrossRef]
48. Schneider, C.A.; Rasband, W.S.; Eliceiri, K.W. NIH Image to ImageJ: 25 years of image analysis. *Nat. Methods* **2012**, *9*, 671–675. [CrossRef]
49. Livak, K.J.; Schmittgen, T.D. Analysis of Relative Gene Expression Data Using RealTime Quantitative PCR and the $2^{-\Delta\Delta CT}$ Method. *Methods* **2001**, *25*, 402–408. [CrossRef] [PubMed]
50. Mani, S.A.; Guo, W.; Liao, M.J.; Eaton, E.N.; Ayyanan, A.; Zhou, A.Y.; Brooks, M.; Reinhard, F.; Zhang, C.C.; Shipitsin, M.; et al. The Epithelial-Mesenchymal Transition Generates Cells with Properties of Stem Cells. *Cell* **2008**, *133*, 704–715. [CrossRef] [PubMed]
51. Arvidsson, S.; Kwasniewski, M.; Riano-Pachon, D.M.; Mueller-Roeber, B. QuantPrime - a flexible tool for reliable high-throughput primer design for quantitative PCR. *BMC Bioinform.* **2008**, *9*, 465. [CrossRef] [PubMed]
52. Gubelmann, C.; Gattiker, A.; Massouras, A.; Hens, K.; David, F.; Decouttere, F.; Rougemont, J.; Deplancke, B. GETPrime: A gene- or transcript-specific primer database for quantitative real-time PCR. *Database* **2011**, *2011*, bar040. [CrossRef]
53. Soule, H.D.; Maloney, T.M.; Wolman, S.R.; Peterson, W.D.; Brenz, R.; McGrath, C.M.; Russo, J.; Pauley, R.J.; Jones, R.F.; Brooks, S.C. Isolation and Characterization of a Spontaneously Immortalized Human Breast Epithelial Cell Line, MCF-10. *Cancer Res.* **1990**, *50*, 6075–6086. [PubMed]
54. Bello, D. Androgen responsive adult human prostatic epithelial cell lines immortalized by human papillomavirus 18. *Carcinogenesis* **1997**, *18*, 1215–1223. [CrossRef] [PubMed]
55. Chaiswing, L.; Zhong, W.; Oberley, T.D. Distinct Redox Profiles of Selected Human Prostate Carcinoma Cell Lines: Implications for Rational Design of Redox Therapy. *Cancers* **2011**, *3*, 3557–3584. [CrossRef] [PubMed]
56. Dawson, P.J.; Wolman, S.R.; Tait, L.; Heppner, G.H.; Miller, F.R. MCF10AT: A model for the evolution of cancer from proliferative breast disease. *Am. J. Pathol.* **1996**, *148*, 313–319.
57. Gross, S.M.; Dane, M.A.; Smith, R.L.; Devlin, K.L.; McLean, I.C.; Derrick, D.S.; Mills, C.E.; Subramanian, K.; London, A.B.; Torre, D.; et al. A multi-omic analysis of MCF10A cells provides a resource for integrative assessment of ligand-mediated molecular and phenotypic responses. *Commun. Biol.* **2022**, *5*, 1–20. [CrossRef]
58. Muñoz-Moreno, L.; Carmena, M.J.; Prieto, J.C.; Schally, A.V.; Bajo, A.M. Tumorigenic transformation of human prostatic epithelial cell line RWPE-1 by growth hormone-releasing hormone (GHRH). *Prostate* **2022**, *82*, 933–941. [CrossRef]
59. Qu, Y.; Han, B.; Yu, Y.; Yao, W.; Bose, S.; Karlan, B.Y.; Giuliano, A.E.; Cui, X. Evaluation of MCF10A as a reliable model for normal human mammary epithelial cells. *PLoS ONE* **2015**, *10*, e0131285. [CrossRef] [PubMed]
60. Santner, S.J.; Dawson, P.J.; Tait, L.; Soule, H.D.; Eliason, J.; Mohamed, A.N.; Wolman, S.R.; Heppner, G.H.; Miller, F.R. Malignant MCF10CA1 Cell Lines Derived from Premalignant Human Breast Epithelial MCF10AT Cells. *Breast Cancer Res. Treat.* **2001**, *65*, 101–110. [CrossRef] [PubMed]
61. Benson, P.J.; Smith, C.S. Cytomegalovirus prostatitis. *Urology* **1992**, *40*, 165–167. [CrossRef] [PubMed]
62. Samanta, M.; Harkins, L.; Klemm, K.; Britt, W.J.; Cobbs, C.S. High Prevalence of Human Cytomegalovirus in Prostatic Intraepithelial Neoplasia and Prostatic Carcinoma. *J. Urol.* **2003**, *170*, 998–1002. [CrossRef] [PubMed]
63. Ridge, K.M.; Eriksson, J.E.; Pekny, M.; Goldman, R.D. Roles of vimentin in health and disease. *Genes Dev.* **2022**, *36*, 391–407. [CrossRef] [PubMed]

64. Steinert, P.M.; Roop, D.R. Molecular and Cellular Biology of Intermediate Filaments. *Annu. Rev. Biochem.* **1988**, *57*, 593–625. [CrossRef]
65. Vuoriluoto, K.; Haugen, H.; Kiviluoto, S.; Mpindi, J.P.; Nevo, J.; Gjerdrum, C.; Tiron, C.; Lorens, J.B.; Ivaska, J. Vimentin regulates EMT induction by Slug and oncogenic H-Ras and migration by governing Axl expression in breast cancer. *Oncogene* **2011**, *30*, 1436–1448. [CrossRef]
66. Zeisberg, M.; Neilson, E.G. Biomarkers for epithelial-mesenchymal transitions. *J. Clin. Investig.* **2009**, *119*, 1429–1437. [CrossRef]
67. Liu, Y.; Mi, Y.; Mueller, T.; Kreibich, S.; Williams, E.G.; Van Drogen, A.; Borel, C.; Frank, M.; Germain, P.L.; Bludau, I.; et al. Multi-omic measurements of heterogeneity in HeLa cells across laboratories. *Nat. Biotechnol.* **2019**, *37*, 314–322. [CrossRef]
68. Lim, J.; Thiery, J.P. Epithelial-mesenchymal transitions: Insights from development. *Development* **2012**, *139*, 3471–3486. [CrossRef]
69. Nieto, M.A. Epithelial Plasticity: A Common Theme in Embryonic and Cancer Cells. *Science* **2013**, *342*, 1234850. [CrossRef] [PubMed]
70. Scheibner, K.; Schirge, S.; Burtscher, I.; Büttner, M.; Sterr, M.; Yang, D.; Böttcher, A.; Ansarullah.; Irmler, M.; Beckers, J.; et al. Epithelial cell plasticity drives endoderm formation during gastrulation. *Nat. Cell Biol.* **2021**, *23*, 692–703. [CrossRef] [PubMed]
71. Thiery, J.P.; Acloque, H.; Huang, R.Y.; Nieto, M.A. Epithelial-Mesenchymal Transitions in Development and Disease. *Cell* **2009**, *139*, 871–890. [CrossRef] [PubMed]
72. Korpal, M.; Lee, E.S.; Hu, G.; Kang, Y. The miR-200 Family Inhibits Epithelial-Mesenchymal Transition and Cancer Cell Migration by Direct Targeting of E-cadherin Transcriptional Repressors ZEB1 and ZEB2. *J. Biol. Chem.* **2008**, *283*, 14910–14914. [CrossRef] [PubMed]
73. Li, R.; Liang, J.; Ni, S.; Zhou, T.; Qing, X.; Li, H.; He, W.; Chen, J.; Li, F.; Zhuang, Q.; et al. A Mesenchymal-to-Epithelial Transition Initiates and Is Required for the Nuclear Reprogramming of Mouse Fibroblasts. *Cell Stem Cell* **2010**, *7*, 51–63. [CrossRef] [PubMed]
74. Pattabiraman, D.R.; Bierie, B.; Kober, K.I.; Thiru, P.; Krall, J.A.; Zill, C.; Reinhardt, F.; Tam, W.L.; Weinberg, R.A. Activation of PKA leads to mesenchymal-to-epithelial transition and loss of tumor-initiating ability. *Science* **2016**, *351*, aad3680. [CrossRef] [PubMed]
75. Samavarchi-Tehrani, P.; Golipour, A.; David, L.; Sung, H.k.; Beyer, T.A.; Datti, A.; Woltjen, K.; Nagy, A.; Wrana, J.L. Functional Genomics Reveals a BMP-Driven Mesenchymal-to-Epithelial Transition in the Initiation of Somatic Cell Reprogramming. *Cell Stem Cell* **2010**, *7*, 64–77. [CrossRef]
76. Watanabe, K.; Liu, Y.; Noguchi, S.; Murray, M.; Chang, J.C.; Kishima, M.; Nishimura, H.; Hashimoto, K.; Minoda, A.; Suzuki, H. OVOL2 induces mesenchymal-to-epithelial transition in fibroblasts and enhances cell-state reprogramming towards epithelial lineages. *Sci. Rep.* **2019**, *9*, 6490. [CrossRef]
77. Lambert, A.W.; Pattabiraman, D.R.; Weinberg, R.A. Emerging Biological Principles of Metastasis. *Cell* **2017**, *168*, 670–691. [CrossRef]
78. Krebs, A.M.; Mitschke, J.; Lasierra Losada, M.; Schmalhofer, O.; Boerries, M.; Busch, H.; Boettcher, M.; Mougiakakos, D.; Reichardt, W.; Bronsert, P.; et al. The EMT-activator Zeb1 is a key factor for cell plasticity and promotes metastasis in pancreatic cancer. *Nat. Cell Biol.* **2017**, *19*, 518–529. [CrossRef]
79. Kröger, C.; Afeyan, A.; Mraz, J.; Eaton, E.N.; Reinhardt, F.; Khodor, Y.L.; Thiru, P.; Bierie, B.; Ye, X.; Burge, C.B.; et al. Acquisition of a hybrid E/M state is essential for tumorigenicity of basal breast cancer cells. *Proc. Natl. Acad. Sci. USA* **2019**, *116*, 7353–7362. [CrossRef] [PubMed]
80. Lu, M.; Jolly, M.K.; Levine, H.; Onuchic, J.N.; Ben-Jacob, E. MicroRNA-based regulation of epithelial-hybrid-mesenchymal fate determination. *Proc. Natl. Acad. Sci. USA* **2013**, *110*, 18144–18149. [CrossRef] [PubMed]
81. Lüönd, F.; Sugiyama, N.; Bill, R.; Bornes, L.; Hager, C.; Tang, F.; Santacroce, N.; Beisel, C.; Ivanek, R.; Bürglin, T.; et al. Distinct contributions of partial and full EMT to breast cancer malignancy. *Dev. Cell* **2021**, *56*, 3203–3221.e11. [CrossRef] [PubMed]
82. Saitoh, M. Involvement of partial EMT in cancer progression. *J. Biochem.* **2018**, *164*, 257–264. [CrossRef]
83. Batlle, E.; Sancho, E.; Francí, C.; Domínguez, D.; Monfar, M.; Baulida, J.; García de Herreros, A. The transcription factor Snail is a repressor of E-cadherin gene expression in epithelial tumour cells. *Nat. Cell Biol.* **2000**, *2*, 84–89. [CrossRef]
84. Cano, A.; Pérez-Moreno, M.A.; Rodrigo, I.; Locascio, A.; Blanco, M.J.; del Barrio, M.G.; Portillo, F.; Nieto, M.A. The transcription factor Snail controls epithelial–mesenchymal transitions by repressing E-cadherin expression. *Nat. Cell Biol.* **2000**, *2*, 76–83. [CrossRef] [PubMed]
85. Nieto, M.A.; Bennett, M.F.; Sargent, M.G.; Wilkinson, D.G. Cloning and developmental expression of Sna, a murine homologue of the Drosophila snail gene. *Development* **1992**, *116*, 227–237. [CrossRef] [PubMed]
86. Smith, D.E.; Amo, F.F.D.; Gridley, T. Isolation of Sna, a mouse gene homologous to the Drosophila genes snail and escargot: Its expression pattern suggests multiple roles during postimplantation development. *Development* **1992**, *116*, 1033–1039. [CrossRef]
87. Fu, H.; Qi, L.; Chen, L.; He, Y.; Zhang, N.; Guo, H. Expression of Ovol2 is related to epithelial characteristics and shows a favorable clinical outcome in hepatocellular carcinoma. *OncoTargets Ther.* **2016**, *9*, 5963–5973. [CrossRef]
88. Kitazawa, K.; Hikichi, T.; Nakamura, T.; Mitsunaga, K.; Tanaka, A.; Nakamura, M.; Yamakawa, T.; Furukawa, S.; Takasaka, M.; Goshima, N.; et al. OVOL2 Maintains the Transcriptional Program of Human Corneal Epithelium by Suppressing Epithelial-to-Mesenchymal Transition. *Cell Rep.* **2016**, *15*, 1359–1368. [CrossRef]
89. Li, B.; Dai, Q.; Li, L.; Nair, M.; Mackay, D.R.; Dai, X. Ovol2, a Mammalian Homolog of Drosophila ovo: Gene Structure, Chromosomal Mapping, and Aberrant Expression in Blind-Sterile Mice. *Genomics* **2002**, *80*, 319–325. [CrossRef] [PubMed]

90. Roca, H.; Hernandez, J.; Weidner, S.; McEachin, R.C.; Fuller, D.; Sud, S.; Schumann, T.; Wilkinson, J.E.; Zaslavsky, A.; Li, H.; et al. Transcription Factors OVOL1 and OVOL2 Induce the Mesenchymal to Epithelial Transition in Human Cancer. *PLoS ONE* **2013**, *8*, e76773. [CrossRef] [PubMed]
91. Ahler, E.; Sullivan, W.J.; Cass, A.; Braas, D.; York, A.G.; Bensinger, S.J.; Graeber, T.G.; Christofk, H.R. Doxycycline Alters Metabolism and Proliferation of Human Cell Lines. *PLoS ONE* **2013**, *8*, e64561. [CrossRef] [PubMed]
92. Chatzispyrou, I.A.; Held, N.M.; Mouchiroud, L.; Auwerx, J.; Houtkooper, R.H. Tetracycline Antibiotics Impair Mitochondrial Function and Its Experimental Use Confounds Research. *Cancer Res.* **2015**, *75*, 4446–4449. [CrossRef] [PubMed]
93. Moullan, N.; Mouchiroud, L.; Wang, X.; Ryu, D.; Williams, E.G.; Mottis, A.; Jovaisaite, V.; Frochaux, M.V.; Quiros, P.M.; Deplancke, B.; et al. Tetracyclines Disturb Mitochondrial Function across Eukaryotic Models: A Call for Caution in Biomedical Research. *Cell Rep.* **2015**, *10*, 1681–1691. [CrossRef] [PubMed]
94. Grisanti, S.; Guidry, C. Transdifferentiation of retinal pigment epithelial cells from epithelial to mesenchymal phenotype. *Investig. Ophthalmol. Vis. Sci.* **1995**, *36*, 391–405.
95. Shih, Y.H.; Radeke, M.J.; Radeke, C.M.; Coffey, P.J. Restoration of Mesenchymal RPE by Transcription Factor-Mediated Reprogramming. *Investig. Ophthalmol. Vis. Sci.* **2017**, *58*, 430–441. [CrossRef] [PubMed]
96. Ciferri, C.; Chandramouli, S.; Donnarumma, D.; Nikitin, P.A.; Cianfrocco, M.A.; Gerrein, R.; Feire, A.L.; Barnett, S.W.; Lilja, A.E.; Rappuoli, R.; et al. Structural and biochemical studies of HCMV gH/gL/gO and Pentamer reveal mutually exclusive cell entry complexes. *Proc. Natl. Acad. Sci. USA* **2015**, *112*, 1767–1772. [CrossRef]
97. Gerna, G.; Revello, M.G.; Baldanti, F.; Percivalle, E.; Lilleri, D. The pentameric complex of human Cytomegalovirus: Cell tropism, virus dissemination, immune response and vaccine development. *J. Gen. Virol.* **2017**, *98*, 2215–2234. [CrossRef]
98. Kabanova, A.; Marcandalli, J.; Zhou, T.; Bianchi, S.; Baxa, U.; Tsybovsky, Y.; Lilleri, D.; Silacci-Fregni, C.; Foglierini, M.; Fernandez-Rodriguez, B.M.; et al. Platelet-derived growth factor-α receptor is the cellular receptor for human cytomegalovirus gHgLgO trimer. *Nat. Microbiol.* **2016**, *1*, 1–8. [CrossRef]
99. Kschonsak, M.; Johnson, M.C.; Schelling, R.; Green, E.M.; Rougé, L.; Ho, H.; Patel, N.; Kilic, C.; Kraft, E.; Arthur, C.P.; et al. Structural basis for HCMV Pentamer receptor recognition and antibody neutralization. *Sci. Adv.* **2022**, *8*, eabm2536. [CrossRef] [PubMed]
100. Kschonsak, M.; Rougé, L.; Arthur, C.P.; Hoangdung, H.; Patel, N.; Kim, I.; Johnson, M.C.; Kraft, E.; Rohou, A.L.; Gill, A.; et al. Structures of HCMV Trimer reveal the basis for receptor recognition and cell entry. *Cell* **2021**, *184*, 1232–1244.e16. [CrossRef] [PubMed]
101. Nguyen, C.C.; Kamil, J.P. Pathogen at the Gates: Human Cytomegalovirus Entry and Cell Tropism. *Viruses* **2018**, *10*, 704. [CrossRef] [PubMed]
102. O'Connor, C.M.; Shenk, T. Human Cytomegalovirus pUS27 G Protein-Coupled Receptor Homologue Is Required for Efficient Spread by the Extracellular Route but Not for Direct Cell-to-Cell Spread. *J. Virol.* **2011**, *85*, 3700–3707. [CrossRef] [PubMed]
103. Towler, J.C.; Ebrahimi, B.; Lane, B.; Davison, A.J.; Dargan, D.J. Human cytomegalovirus transcriptome activity differs during replication in human fibroblast, epithelial and astrocyte cell lines. *J. Gen. Virol.* **2012**, *93*, 1046–1058. [CrossRef] [PubMed]
104. Sinzger, C.; Schmidt, K.; Knapp, J.; Kahl, M.; Beck, R.; Waldman, J.; Hebart, H.; Einsele, H.; Jahn, G. Modification of human cytomegalovirus tropism through propagation in vitro is associated with changes in the viral genome. *J. Gen. Virol.* **1999**, *80*, 2867–2877. [CrossRef]
105. Stanton, R.J.; Baluchova, K.; Dargan, D.J.; Cunningham, C.; Sheehy, O.; Seirafian, S.; McSharry, B.P.; Neale, M.L.; Davies, J.A.; Tomasec, P.; et al. Reconstruction of the complete human cytomegalovirus genome in a BAC reveals RL13 to be a potent inhibitor of replication. *J. Clin. Investig.* **2010**, *120*, 3191–3208. [CrossRef]
106. Wang, D.; Shenk, T. Human Cytomegalovirus UL131 Open Reading Frame Is Required for Epithelial Cell Tropism. *J. Virol.* **2005**, *79*, 10330–10338. [CrossRef]
107. Al Qaffas, A.; Camiolo, S.; Vo, M.; Aguiar, A.; Ourahmane, A.; Sorono, M.; Davison, A.J.; McVoy, M.A.; Hertel, L. Genome sequences of human cytomegalovirus strain TB40/E variants propagated in fibroblasts and epithelial cells. *Virol. J.* **2021**, *18*, 112. [CrossRef]
108. Buckner, A.E.; Dix, R.D. Nicotine Treatment Alters NF-κB Expression in Human Cytomegalovirus-Infected ARPE-19 Cells. *Curr. Eye Res.* **2006**, *31*, 191–198. [CrossRef]
109. Corcoran, K.; Sherrod, C.J.; Perkowski, E.F.; Texier, J.; Li, F.; Wang, I.M.; McVoy, M.; Fu, T.M.; Dittmer, D.P. Genome Sequences of Diverse Human Cytomegalovirus Strains with Utility in Drug Screening and Vaccine Evaluation. *Genome Announc.* **2017**, *5*, e01433-16. [CrossRef] [PubMed]
110. García-Ríos, E.; Rodríguez, M.J.; Terrón, M.C.; Luque, D.; Pérez-Romero, P. Identification and Characterization of Epithelial Cell-Derived Dense Bodies Produced upon Cytomegalovirus Infection. *Vaccines* **2022**, *10*, 1308. [CrossRef] [PubMed]
111. Gerna, G.; Lilleri, D.; Fornara, C.; Bruno, F.; Gabanti, E.; Cane, I.; Furione, M.; Revello, M.G. Differential kinetics of human cytomegalovirus load and antibody responses in primary infection of the immunocompetent and immunocompromised host. *J. Gen. Virol.* **2015**, *96*, 360–369. [CrossRef] [PubMed]
112. Gerna, G.; Percivalle, E.; Perez, L.; Lanzavecchia, A.; Lilleri, D. Monoclonal Antibodies to Different Components of the Human Cytomegalovirus (HCMV) Pentamer gH/gL/pUL128L and Trimer gH/gL/gO as well as Antibodies Elicited during Primary HCMV Infection Prevent Epithelial Cell Syncytium Formation. *J. Virol.* **2016**, *90*, 6216–6223. [CrossRef] [PubMed]

113. Giménez, E.; Blanco-Lobo, P.; Muñoz-Cobo, B.; Solano, C.; Amat, P.; Pérez-Romero, P.; Navarro, D. Role of cytomegalovirus (CMV)-specific polyfunctional CD8+ T-cells and antibodies neutralizing virus epithelial infection in the control of CMV infection in an allogeneic stem-cell transplantation setting. *J. Gen. Virol.* **2015**, *96*, 2822–2831. [CrossRef] [PubMed]
114. Huber, M.T.; Tomazin, R.; Wisner, T.; Boname, J.; Johnson, D.C. Human Cytomegalovirus US7, US8, US9, and US10 Are Cytoplasmic Glycoproteins, Not Found at Cell Surfaces, and US9 Does Not Mediate Cell-to-Cell Spread. *J. Virol.* **2002**, *76*, 5748–5758. [CrossRef] [PubMed]
115. Maidji, E.; Tugizov, S.; Jones, T.; Zheng, Z.; Pereira, L. Accessory human cytomegalovirus glycoprotein US9 in the unique short component of the viral genome promotes cell-to-cell transmission of virus in polarized epithelial cells. *J. Virol.* **1996**, *70*, 8402–8410. [CrossRef]
116. Nogalski, M.T.; Shenk, T. HSATII RNA is induced via a noncanonical ATM-regulated DNA damage response pathway and promotes tumor cell proliferation and movement. *Proc. Natl. Acad. Sci. USA* **2020**, *117*, 31891–31901. [CrossRef]
117. Nogalski, M.T.; Solovyov, A.; Kulkarni, A.S.; Desai, N.; Oberstein, A.; Levine, A.J.; Ting, D.T.; Shenk, T.; Greenbaum, B.D. A tumor-specific endogenous repetitive element is induced by herpesviruses. *Nat. Commun.* **2019**, *10*, 90. [CrossRef]
118. O'Connor, C.M.; Shenk, T. Human Cytomegalovirus pUL78 G Protein-Coupled Receptor Homologue Is Required for Timely Cell Entry in Epithelial Cells but Not Fibroblasts. *J. Virol.* **2012**, *86*, 11425–11433. [CrossRef]
119. Ryckman, B.J.; Chase, M.C.; Johnson, D.C. HCMV gH/gL/UL128-131 interferes with virus entry into epithelial cells: Evidence for cell type-specific receptors. *Proc. Natl. Acad. Sci. USA* **2008**, *105*, 14118–14123. [CrossRef] [PubMed]
120. Tugizov, S.; Maidji, E.; Xiao, J.; Pereira, L. An acidic cluster in the cytosolic domain of human cytomegalovirus glycoprotein B is a signal for endocytosis from the plasma membrane. *J. Virol.* **1999**, *73*, 8677–8688. [CrossRef] [PubMed]
121. Vo, M.; Aguiar, A.; McVoy, M.A.; Hertel, L. Cytomegalovirus Strain TB40/E Restrictions and Adaptations to Growth in ARPE-19 Epithelial Cells. *Microorganisms* **2020**, *8*, 615. [CrossRef] [PubMed]
122. Zhou, X.; Cimato, G.; Zhou, Y.; Frascaroli, G.; Brune, W. A Virus Genetic System to Analyze the Fusogenicity of Human Cytomegalovirus Glycoprotein B Variants. *Viruses* **2023**, *15*, 979. [CrossRef] [PubMed]
123. Braspenning, S.E.; Sadaoka, T.; Breuer, J.; Verjans, G.M.G.M.; Ouwendijk, W.J.D.; Depledge, D.P. Decoding the Architecture of the Varicella-Zoster Virus Transcriptome. *mBio* **2020**, *11*, 1110–1128. [CrossRef] [PubMed]
124. Farnsworth, A.; Johnson, D.C. Herpes Simplex Virus gE/gI Must Accumulate in the trans-Golgi Network at Early Times and Then Redistribute to Cell Junctions To Promote Cell-Cell Spread. *J. Virol.* **2006**, *80*, 3167–3179. [CrossRef] [PubMed]
125. Ouwendijk, W.J.D.; Dekker, L.J.M.; van den Ham, H.J.; Lenac Rovis, T.; Haefner, E.S.; Jonjic, S.; Haas, J.; Luider, T.M.; Verjans, G.M.G.M. Analysis of Virus and Host Proteomes during Productive HSV-1 and VZV Infection in Human Epithelial Cells. *Front. Microbiol.* **2020**, *11*, 1179. [CrossRef]
126. Smith, J.R.; Todd, S.; Ashander, L.M.; Charitou, T.; Ma, Y.; Yeh, S.; Crozier, I.; Michael, M.Z.; Appukuttan, B.; Williams, K.A.; et al. Retinal Pigment Epithelial Cells are a Potential Reservoir for Ebola Virus in the Human Eye. *Transl. Vis. Sci. Technol.* **2017**, *6*, 12. [CrossRef]
127. Ashander, L.M.; Lumsden, A.L.; Dawson, A.C.; Ma, Y.; Ferreira, L.B.; Oliver, G.F.; Appukuttan, B.; Carr, J.M.; Smith, J.R. Infection of Human Retinal Pigment Epithelial Cells with Dengue Virus Strains Isolated during Outbreaks in Singapore. *Microorganisms* **2022**, *10*, 310. [CrossRef]
128. Russo, C.A.; Torti, M.F.; Marquez, A.B.; Sepúlveda, C.S.; Alaimo, A.; García, C.C. Antiviral bioactivity of resveratrol against Zika virus infection in human retinal pigment epithelial cells. *Mol. Biol. Rep.* **2021**, *48*, 5379–5392. [CrossRef]
129. Singh, P.K.; Guest, J.M.; Kanwar, M.; Boss, J.; Gao, N.; Juzych, M.S.; Abrams, G.W.; Yu, F.S.; Kumar, A. Zika virus infects cells lining the blood-retinal barrier and causes chorioretinal atrophy in mouse eyes. *JCI Insight* **2017**, *2*. [CrossRef] [PubMed]
130. Uppal, S.; Postnikova, O.A.; Poliakov, E.; Rogozin, I.; Villasmil, R.; Redmond, T.M. Dissecting the entry mechanisms of SARS-CoV-2 in ARPE-19 cells. *Investig. Ophthalmol. Vis. Sci.* **2023**, *64*, 4431.